HHS Public Access

Author manuscript

Acta Biomater. Author manuscript; available in PMC 2024 September 11.

Published in final edited form as:

Acta Biomater. 2023 June ; 163: 287–301. doi:10.1016/j.actbio.2022.10.052.

Early committed polarization of intracellular tension in response to cell shape determines the osteogenic differentiation of mesenchymal stromal cells☆

Ming-Chung Wu[a,1], **Helen Wenshin Yu**[a,b,1], **Yin-Quan Chen**[c], **Meng-Hsin Ou**[a], **Ricardo Serrano**[d,e,f], **Guan-Lin Huang**[a], **Yang-Kao Wang**[g], **Kung-hui Lin**[h], **Yu-Jui Fan**[i], **Chi-Chang Wu**[j], **Juan C. del Álamo**[d,e,k,l], **Arthur Chiou**[b], **Shu Chien**[d], **Jean-Cheng Kuo**[a,c,*]

[a] Institute of Biochemistry and Molecular Biology, National Yang Ming Chiao Tung University, Taipei 11221, Taiwan

[b] Institute of Biophotonics, National Yang Ming Chiao Tung University, Taipei 11221, Taiwan

[c] Cancer Progression Research Center, National Yang Ming Chiao Tung University, Taipei 11221, Taiwan

[d] Department of Bioengineering and Institute of Engineering in Medicine, University of California at San Diego, La Jolla, CA 92093, USA

[e] Department of Mechanical and Aerospace Engineering, University of California at San Diego, La Jolla, CA 92093, USA

[f] Stanford Cardiovascular Institute, Stanford University School of Medicine, Stanford, CA 94305, USA

[g] Department of Cell Biology and Anatomy, National Cheng Kung University, Tainan, 70101, Taiwan

[h] Institute of Physics, Academia Sinica, Taipei 11529, Taiwan

[i] School of Biomedical Engineering, Taipei Medical University, Taipei 110, Taiwan

[j] Department of Electronic Engineering, National Chin-Yi University of Technology, Taichung 411030, Taiwan

[k] Center for Cardiovascular Biology, University of Washington, School of Medicine, Seattle, WA, 98109, USA

[l] Mechanical Engineering Department, University of Washington, Seattle, WA, 98195, USA

☆Part of the Special Issue on the Mechanics of Cells and Fibers, guest-edited by Professors Amrinder S. Nain, Derrick Dean, and Guy M. Genin.

* Corresponding author. jckuo@nycu.edu.tw (J.-C. Kuo).

[1]These authors contribute equally

Declaration of Competing Interest

The authors declare that they have no conflict of interest.

Supplementary materials

Supplementary material associated with this article can be found, in the online version, at doi: 10.1016/j.actbio.2022.10.052.

Abstract

Within the heterogeneous tissue architecture, a comprehensive understanding of how cell shapes regulate cytoskeletal mechanics by adjusting focal adhesions (FAs) signals to correlate with the lineage commitment of mesenchymal stromal cells (MSCs) remains obscure. Here, via engineered extracellular matrices, we observed that the development of mature FAs, coupled with a symmetrical pattern of radial fiber bundles, appeared at the right-angle vertices in cells with square shape. While circular cells aligned the transverse fibers parallel to the cell edge, and moved them centripetally in a counter-clockwise direction, symmetrical bundles of radial fibers at the vertices of square cells disrupted the counter-clockwise swirling and bridged the transverse fibers to move centripetally. In square cells, the contractile force, generated by the myosin IIA-enriched transverse fibers, were concentrated and transmitted outwards along the symmetrical bundles of radial fibers, to the extracellular matrix through FAs, and thereby driving FA organization and maturation. The symmetrical radial fiber bundles concentrated the transverse fibers contractility inward to the linkage between the actin cytoskeleton and the nuclear envelope. The tauter cytoskeletal network adjusted the nuclear-actomyosin force balance to cause nuclear deformability and to increase nuclear translocation of the transcription co-activator YAP, which in turn modulated the switch in MSC commitment. Thus, FAs dynamically respond to geometric cues and remodel actin cytoskeletal network to re-distribute intracelluar tension towards the cell nucleus, and thereby controlling YAP mechanotransduction signaling in regulating MSC fate decision.

Keywords

Focal adhesions; Geometric cue; Mesenchymal stromal cells; Osteogenesis; Contractile force

1. Introduction

Bone marrow-derived mesenchymal stromal cells (MSCs) are omnipotent cells capable of self-renewal and differentiation into a variety of cell types [1–7]. Thus, MSCs not only contribute to homeostasis [8] but also serve as an attractive cell source for cell therapy to treat various types of diseases and injuries [7,9,10]. In the adult skeleton, MSCs differentiate mainly into osteoblasts and adipocytes. Maintaining the balance along this differentiation axis is crucial for bone stability [11–14]. However, the differentiation lineage of MSCs is influenced by a range of complex physical cues within their local microenvironment, including substrate composition [15,16], stiffness [17], applied strain [18], and geometric features [5,19–22]. Microengineering techniques that geometrically pattern the microenvironment of MSCs have been applied to demonstrate the importance of cell shape and cell size in directing the fates of MSCs [5,19–23]. While tension is a common explanation for cell fate decisions, a comprehensive study to explain how geometric cues guide the cytoskeletal tension via cell adhesive organelles, to modulates the nucleus, and to dictate the differentiation signals in MSCs, has not yet been established.

The adhesive organelles that sense and transduce the mechanical signals from the microenvironment are focal adhesions (FAs) [24–27]. FAs start to form when their central component, the integrin receptor, is activated by engaging with the extracellular matrix

(ECM), followed by the recruitment of FA-associated proteins of various types that connect with the actin cytoskeleton [24,26–30]. Subsequently, FA maturation induces the growth of FAs and changes their composition that either lead to FA stabilization or trigger their disassembly [31–35]. Controlling the maturation state of FAs is crucial to specifying MSC differentiation because different maturation states - modulated by tissue-level ECM elasticity - determine the differentiation of MSCs into a variety of different lineages, such as neuronal cells, muscle cells, or bone cells [17]. FA maturation involves FA size growth and a hierarchical cascade of changes in the abundance of several protein groups that transduce distinct and specific biological signals [32,33,36]. These changes in FA composition affect the organization of the actin cytoskeleton, cell stiffness, and the osteogenic commitment of MSCs [37]. FA signaling, modulated by microenvironmental cues, can change FA organization, cytoskeletal mechanics, cell shape and bring about MSC commitment to either the osteoblast lineage or the adipocyte lineage.

While mature FAs and increased actomyosin contractility have been demonstrated as important effectors of MSC osteogenic differentiation, the regulatory mechanisms of how mechanicallystimulated FAs signal to nucleus in differentiation is not yet established. By imposing geometric constraints on cell shape via micropatterning, we have observed that FAs respond to the geometric signals by modulating their protein composition. Furthermore, FAs guide the orientation of the actin architecture to adjust the distribution of intracellular tension, which reaches the cell nucleus. These biomechanical adjustments modify cell nuclear shape and stiffness, and eventually determine the differentiation fate of the MSCs.

2. Materials and methods

2.1. Cell culture

Human mesenchymal stromal cells (MSCs) from three different donors were purchased from Lonza (PT-2501). Cells were cultured in DMEM (low glucose) supplemented with 10% FBS and 1% penicillin/streptomycin. Only early passage MSCs (from passages 4~6) were used. MSCs were plated at ~ 2,000 cells/cm^2 on 2D micropatterns. MSC differentiation was carried out as described previously [37,38]. The osteogenesis induction medium (OIM) contained 0.1 μM dexamethasone, 5 mM β-glycerophosphate, 50 μM L-ascorbic-2-phosphate in culture medium. The adipogenesis induction medium (AIM) contained 1 μM dexamethasone, 0.5 mM 3-isobutyl-1-methylxanthine, 10 μg/ml insulin, 100 μM indomethasin in culture medium. Mixed differentiation medium contained 1:1 OIM:AIM [5,20]. To inhibit cell proliferation, cells were treated with mitomycin C (2.5 μg/ml; Sigma) for 2 hrs and washed three times with culture medium. Transient transfections were performed by nucleofection (Lonza) using Human MSC Nucleofector Kit and program U-23.

2.2. Plasmids and reagents

Plasmids: GFP-Nesprin-2 (ΔN)-klarischt sequence (GFP-KASH) was kindly provided from Dr. Catherine M. Shanahan laboratory (University of Cambridge, UK).

Antibodies for immunofluorescence: mouse anti-paxillin (BD 610052; dilution: 1/1000), rabbit anti-paxillin (Genetex GTX125891; dilution: 1/100), rabbit anti-vimentin (Genetex GTX100619; dilution: 1/1000), rabbit anti-cortactin (Genetex GTX100253; dilution: 1:500), mouse anti-α-tubulin (Sigma T5168; dilution: 1/2000), rabbit anti-YAP (GeneTex GTX129151; dilution: 1/200), mouse anti-zyxin (Abnova H00007791; dilution: 1/50), mouse anti-vinculin (Sigma V4505; dilution: 1/50), mouse anti-integrin β1 (active form) (Millipore MAB2259Z; dilution: 1/100), rabbit anti-non-muscle myosin IIA (NMIIA) (Genetex GTX101751; dilution: 1/50), rabbit anti-MLC (Cell signaling 3672; dilution: 1/100), mouse anti-pS19-MLC (Cell Signaling 3675; dilution: 1/100), mouse anti-α-actinin (Cell signaling 3134; dilution: 1/25), rabbit anti-pY31-paxillin (Invitrogen 44–720G; dilution: 1/50), mouse anti-fibronectin (Santa cruz sc-8422; dilution: 1/100), mouse anti-Runx2 (Abnova H00000860-M06; dilution: 1/100), mouse anti-PPARγ (Santa cruz sc-166731; dilution: 1/50), rabbit anti-DLX5 (Atlas HPA005670; dilution: 1/200), Alexa Fluor 488 phalloidin (Invitrogen A12379; dilution: 1/500), Alexa Fluor 488-anti-rabbit IgG (Invitrogen A11034; dilution: 1/300), Alexa Fluor 488-anti-mouse IgG (Invitrogen A11029; dilution: 1/300), Alexa Fluor 568-anti-mouse IgG (Invitrogen A11031; dilution: 1/300), Alexa Fluor 568-anti-rabbit IgG (Invitrogen A11036; dilution: 1/300), DAPI (Invitrogen D1306; dilution: 1/300).

Antibodies for blocking assay: mouse anti-integrin β1 (Millipore MAB1987; final conc.: 0.6 μg/ml), mouse anti-integrin β3 (Merck MAB2023Z; final conc.: 1 μg/ml).

Reagents: Nocodazole (10 μM; Sigma); Cytochalasin D (10 μM; Sigma); Latrunculin A (2 μM; Thermo Fisher); Blebbistatin (50 μM; TRC); Y27632 (10 μM; APEXBIO).

2.3. MSC staining for ALP activity and lipid droplets

The protocol for MSC staining was carried out as described previously [5,37]. Cells were fixed in 4% paraformaldehyde, rinsed in PBS and then stained with Fast BCIP/NBT (Sigma) to detect alkaline phosphatase (ALP) activity. Subsequently, the cells were rinsed in 60% isopropanol, stained with 30 mg/ml Oil red O (Sigma) in 60% isopropanol to detect lipid, and finally rinsed in PBS. Cells were then stained with DAPI in PBS to allow us to micrograph and count the total number of cells using a Nikon Eclipse TE100.

2.4. Fabrication of the micropatterned substrates

The protocol for the fabrication of micropatterned substrates on PDMS was carried out as described previously [39]. Briefly, PDMS stamps were cast, baked and removed from their silicon wafers (master templates), which were fabricated by photolithographic methods. The surface of the PDMS stamps was coated with fibronectin (50 μg/ml; CHIA SON CELL TECH. CORP.) for 1 hr, washed with sterilized ddH_2O, and dried with compressed air. A glass coverslip spin-coated with PDMS was UV oxidized for 10 min (UVO cleaner 42; Jelight), and then placed in contact with a PDMS stamps for 5 min in order to transfer the fibronectin. The coverslips were then blocked with 0.2% Pluronic® F-127 (Sigma) for 1hr, and rinsed three times with PBS before MSC seeding.

2.5. Traction force microscopy and monolayer stress microscopy

MSCs were seeded on polyacrylamide gels coated with the micropatterned fibronectin. The protocol of fabricating the micropatterned substrates on the elastic polyacrylamide gel was carried out as described previously [40]. In brief, PDMS stamps generated from the silicon wafers (master templates) were coated with fibronectin (50 μg/ml; CHIA SON CELL TECH. CORP.). A glass coverslip (18 × 18 mm^2) was coated with PLL-PEG for 1hr, UV oxidized for 10 min, then placed in contact with a PDMS stamp to absorb the fibronectin; after this it was blocked with 1% BSA. The fibronectin micropatterned on a template coverslip (18 × 18 mm^2) was transferred onto an acrylamide gel by polymerization of the gel directly on a second glass coverslip (22 × 22 mm^2). The elastic polyacrylamide gels [41] were prepared using a final concentration of acrylamide/Bis-acrylamide of 10%/0.2% in order to produce a 21.5 kPa gel, and then mixed with 200 nm-diameter fluorescent beads (Thermofisher). The substrate deformation field was deduced from the 3D displacements of the fluorescent beads embedded in the gel. The force (pN) and the traction force (Pa) exerted by the cells were determined from the measured substrate deformation via the equation for static equilibrium of an elastic substrate, as described previously [42,43]. In particular, we obtained the traction stresses in the direction parallel to the top surface of the substrate, denoted as in-plane or tangential traction stress vector (t_{xz},t_{yz}), and the stresses perpendicular to that surface (t_{zz}). Using the measured traction stresses as inputs, we calculated the in-plane mechanical stress tensor inside the cells using monolayer stress microscopy, as previously described [44, 45]. From this tensor, we determined the principal directions of stress (eigendirections) and intracellular tension (trace).

2.6. Video particle tracking microrheology

MSCs seeded on a 10 cm-diameter tissue culture dish were injected with 200 nm-diameter fluorescent carboxylated polystyrene particles (Thermofisher) via a biolistic particle delivery system (PDS-100, Bio-Rad; pressure 450 psi). The cells were then washed, recovered and plated on PDMS gels fabricated with micropatterned fibronectin. Subsequently, the cells were placed in a temperature-controlled and CO_2-controlled chamber (TOKAI HIT) of an inverted microscope (Ti-E, Nikon). The 2D-Brownian motion of the intra-nuclear fluorescence beads were tracked and recorded for 10 sec using an inverted epi-fluorescence microscope (Ti-E, Nikon) equipped with an oil-immersion objective (Nikon, 100X/ N.A. 1.45) and a CMOS camera (Hamamatsu, OHCA-Flash 4.0) operated by NIS-Elements software (Nikon); the sampling rate was 100 Hz with an image resolution of 130 nm/pixel, and 1024 × 1024 pixels per frame. Brownian motion of the intra-nuclear fluorescence beads was analyzed using a customized MATLAB Program [46,47] to obtain the intra-nuclear elastic properties (the shear elastic modulus G') [48,49], which represents the stiffness of cell nucleus (Pa). We limited our analysis to the range with time lags of 0.01 s < τ < 1 s. To exclude particles that exhibited non-Brownian motion, only the particle trajectories consistent with 0 < α < 1, where "α" is the exponent in the expression mean-squared displacement (MSD) = $<\Delta r^2(\tau)> = D\tau^{\alpha}$ ("D" is the diffusion coefficient), were retained for the calculation of G'.

2.7. Immunofluorescence analysis and image analysis

For cytoskeleton proteins staining (except of NMIIA) and DLX5 staining, the cells were fixed with 4% paraformaldehyde in cytoskeleton buffer (10 mM MES pH6.1, 138 mM KCl, 3 mM $MgCl_2$, 2 mM EGTA) at room temperature for 20 min, permeabilized with cytoskeleton buffer containing 0.5 % Triton X-100 at room temperature for 5 min, and blocked with blocking solution (3% BSA / 0.02% Triton-X100 in PBS) at room temperature for 60 min. Subsequently, the cells were incubated with the indicated primary antibodies in blocking solution at 4 °C for 16 h, and then incubated with fluorescent dye–conjugated secondary antibody at room temperature for 1 h. For NMIIA staining, cells were fixed with fixing buffer I (1.1 mM Na_2HPO_4, 0.4 mM KH_2PO_4, 4 mM $NaHCO_3$, 5 mM PIPES pH6.1, 137 mM NaCl, 5 mM KCl, 5.5 mM Glucose, 2 mM $MgCl_2$, 2 mM EGTA, 0.1% glutaraldehyde, 1% paraformaldehyde, and 0.3% Triton X-100) at 37 °C for 1 min, and continued to be fixed in fixing buffer II (1.1 mM Na_2 HPO_4, 0.4 mM KH_2 PO_4, 4 mM $NaHCO_3$, 5 mM PIPES pH6.1, 137 mM NaCl, 5 mM KCl, 5.5 mM Glucose, 2 mM $MgCl_2$, 2 mM EGTA, 0.5% glutaraldehyde) at 37 °C for 15 min. Subsequently, the cells were blocked with blocking solution (1% BSA/ 0.1% Triton-X100 in PBS) at 37 °C for 10 min, incubated with the NMIIA antibodies in blocking solution at 37 °C for 1 h, and then incubated with fluorescent dye–conjugated secondary antibody at 37 °C for 1 h. For PPARγ staining, the cells were fixed with 4% paraformaldehyde in PBS at room temperature for 20 min. Cell were washed with 0.1 M glycine in PBS for 10 min, permeabilized with PBS containing 0.1 % Triton X-100 at room temperature for 10 min, and blocked with blocking solution (1% BSA in PBS) at room temperature for 60 min. Subsequently, the cells were incubated with the PPARγ antibodies in blocking solution at 4 °C for 16 h, and then incubated with fluorescent dye–conjugated secondary antibody at room temperature for 1 h. Finally, the cells were mounted on a magnetic chamber (LCI) and incubated with PBS containing N-propyl gallate for either confocal, or epi-fluorescence imaging. Confocal images were acquired using an *iLas* multi-modal of TIRF (Roper) / spinning disk confocal (CSUX1, Yokogawa) microscope (Ti-E, Nikon) system equipped with 60X, 1.49NA Plan objective lens (Nikon) and an EMCCD (Andor), and processed using Metamorph software. Epi-fluorescence images were obtained using a microscope (DMRBE, Leica) coupled with a 63X, 1.4NA objective lens (Leica) and an 512B EMCCD (Andor) operated by Micro-Manager 1.4 software (Leica).

To determine the relative intensity of different FA proteins in paxillin-labelled FAs within twelve angular sectors, the double-labeled immunofluorescence images were divide into twelve angular sectors using a customized MATLAB Program. Images of paxillin were thresholded to highlight only the paxillin-labelled FAs, which was used to create a mask. The mask was transferred to the FA protein immunofluorescence image (integrin β1, pY31-paxillin, vinculin, zyxin, or fibronectin) of the same angular sector in the cell. The average intensity of the fluorescence in FAs within one angular sector was calculated as the percentage among twelve angular sectors, and presented graphically using Excel software (Microsoft).

2.8. Time-lapse microscopy

To analyze the dynamics of F-actin, cells expressing GFP-Ftractin were mounted on a magnetic chamber (LCI) and incubated in phenol red-free culture medium with 25 mM Hepes (pH = 7.4) and imaged by confocal using a 40X, 0.75NA objective on the *iLas* multi-modal of TIRF (Roper) / spinning disk confocal (CSUX1, Yokogawa) microscope (Ti-E, Nikon) system described above. Stage temperature was maintained at 37 °C with an airstream incubator (Nevtek) and focus was maintained using the PerfectFocus (™) system (Nikon). Confocal images of GFP-Ftractin were captured at 5 min intervals using a ProEM EMCCD (Princeton).

2.9. Cell spreading assay and image analysis

Cells growing on tissue culture plates were trypsinized and reseeded on fibronectin-coated square islands for 60 min to allow them to adhere and spread. Next the cells were fixed with 4% paraformaldehyde in PBS for 20 min at room temperature and then imaged using a microscope (Eclipse TS100; Nikon) coupled with a 20 × 0.45NA objective lens (Nikon) and a WHITE CCD camera operated by ISCapture software (TUCSEN). To calculate the percentage of cell spreading, we divided the number of cells presenting square shape by the total number of attached cells. The results are presented graphically using Excel software (Microsoft).

2.10. Statistical analysis and data presentation

SPSS was used to test for normality and homoscedasticity. Statistical significance was calculated by either the Student's t-test or the one-way ANOVA. All the graphs were plotted with Excel software (Microsoft).

3. Results

3.1. Geometric cues control mesenchymal stromal cell osteogenesis vs. adipogenesis lineage

We previously demonstrated the effect of integrin-mediated FA signaling on MSC osteogenesis [16,37], but how MSCs respond to their microenvironment with different geometrical shapes through FA signaling and further determine the differentiation lineage remains unknown. To assess the role of the cell shape and mechanics on stem cell commitment, we used microcontact printing techniques (see Materials and Methods) to generate circular and square islands of fibronectin on polydimethylsiloxane (PDMS) substrate (Fig. 1a). The size of the islands, 10000 μm^2, allowed only one single cell to attach and spread within each island. The main geometrical difference between the circular and square islands was the presence of right-angle vertics in the squares. MSCs were plated on the islands, then exposed to a 1:1 combination of adipogenesis and osteogenesis-promoting soluble cues for 14 days. The percentages of cells with ALP activity (osteogenesis marker) or with lipid droplets (adipogenesis marker) were determined for each cell island (Fig. 1b) to quantify the effect of cell shape on MSC commitment. Since ALP activity in preadipocytes was detected in some tissues [50], those cells with double staining for active ALP and lipid droplets were counted as adipogenesis. In Fig. 1c, cells in the circles showed about 40%

(40.14% ± 3.91) osteogenesis, while cells in the squares displayed about 69% (69.14% ± 0.64) osteogenesis. We further examined the expression level of the osteogenic transcription factor Runx2, and found that square cells expressed more Runx2 than circular cells (Fig. 1d). These results suggest that geometric cues can switch MSC commitment between the adipogenic and osteogenic fates.

3.2. MSC commitment varies with changes in focal adhesions

Cell shape changes imposed by geometric cues are sensed by fibronectin-bound integrin receptors associated with FA signaling complexes [33,37]. Thus, we next characterized the effect of geometrical constraints on FA organization. Cells were cultured for 16 h under standard growth conditions or mixed differentiation medium, and then paxillin-stained by immunofluorescence to visualize FAs. These data showed nascent adhesions (small newborn adhesions) at the cell periphery and mature FAs (larger adhesions) forming a radial pattern (Fig. 2a; Fig. S1a). To characterize how FA organization varied across different adhesive geometries, we divided each cell into twelve angular sectors (Fig. 2b) and quantified the length of the FAs found within each sector (Fig. 2c; Fig. S1b). The analysis revealed that FA length was uniform across all angular sectors in circular islands. However, cells adhering to square micropatterns had significantly larger FAs in the vertex sectors (i.e., the 30 °~60 °, 120 °~150 °, −30 °~−60 ° and −120 °~ −150 ° sectors) (Fig. 2c; Fig. S1b). Similar results were obtained with increasing cell culture time in mixed differentiation medium to 14 or 16 days (Fig. S2a).

A previous study using three-dimensional super-resolution fluorescence microscopy has shown that FAs comprise vertical strata containing specific proteins: a membrane-apposed integrin-signalling layer, an intermediate force-transduction layer, and an upper-most actin-regulatory layer [51]. Thus, we sought to clarify the FA molecular architecture within the MSCs growing on circular and square micropatterns. Specifically, we imaged the FA proteins present in the specialized layers to quantify whether their enrichment was dependent on the underlying micropattern geometry. The images revealed that the FA proteins of the integrinsignaling layer (active integrin β1 and pY31-paxillin) and the force-transduction layer (vinculin and zyxin) could be localized at paxillin-marked FAs in MSCs. The fluorescence intensity ratio of the proteins in paxillin-labelled FAs did not vary across the different angular sectors of the circular cells. However, there was a significant accumulation of active integrin β1, pY31-paxillin, vinculin and zyxin at the vertices in the square cells (Fig. 2d). Upon paxillin phosphorylated at Y31, which is signaled by active integrin β1, paxillin acts as a scaffold for vinculin FA recruitment to reinforce cytoskeletal-ECM linkage and drives FA maturation [52]. We further confirmed the enrichment of pY31-paxillin at the vertices in the differentiated square MSCs (Fig. S1c; Fig. S2b). To gain insight into geometry-mediated growth of fibrillar adhesions, we further imaged fibronectin to reveal fibronectin reorganization in circular and square cells. We detected longer fibrillar adhesions and more fibronectin at paxillin-marked FAs at the vertices in the square cells (Fig. 2e), suggesting that integrin β1 activation regulated by substrate geometry promotes fibronectin reorganization (fibronectin fibrillogenesis) for fibrillar adhesion formation. The graphs show only the results from the first quadrant (0 °~90 °), since the results from the remaining three quadrants were similar. Altogether, the

results indicate that substrate geometry can modulate the molecular architecture of the FAs by manipulating protein density within the integrin-signaling and the force-transduction layers. The resulting stratification imposes spatial constraints on the connections between FAs and the cytoskeleton.

Next, we analyzed the orientation of the specific proteins within the stratified FAs to investigate how geometric constraints influence their interconnections. Immunofluorescence staining of F-actin and paxillin revealed the localization and orientation of the bundled actin filaments and FAs, respectively (Fig. 3a; Fig. S1a; Fig. S1d). We imaged the key proteins of the actin cytoskeleton (F-actin), the FAs (paxillin and active integrin β1), the microtubules (α-tubulin) and the intermediate filaments (vimentin) to measure their orientations. Their orientation was assessed by measuring the angle between the indicated proteins and the cell membrane (Fig. 3b) in three angular sectors of the first quadrant (0 °~90 °) (Fig. 3c). The statistical distribution of the angles revealed that these proteins had significantly different orientations in the circular vs. square MSCs (Fig. 3d; Fig. S1e; Fig. S2c; Fig. S3). In circular cells, the FAs were poorly aligned with F-actin, the microtubules, and vimentin (Fig. 3d; Fig. S1e; Fig. S2c; Fig. S3). In contrast, the alignment was closer for the square cells. In particular, paxillin and active integrin β1 were aligned with F-actin at the vertices, but not with microtubules and vimentin (Fig. 3d; Fig. S1e; Fig. S2c; Fig. S3). Taken as a whole, these findings show that cell shape controls the alignment between the FAs and the cytoskeleton by modulating the composition of the FAs' multilaminar protein architecture.

3.3. Cell shape vertices focus and align cytoskeletal tension

Based on the findings that changes in cell shape affect the organization of FAs and their orientation with respect to cytoskeletal structures, we hypothesized that the cell shape modulates the mechanical forces exerted by MSCs and their intracellular distribution. To test this hypothesis, we characterized the subcellular localization of non-muscle myosin-II heavy chain-A (NMIIA), regulatory light chain of myosin-II (MLC), MLC phosphorylated at Ser 19 (p-MLC), α-actinin and F-actin in MSCs plated on circular and square islands (Fig. 3e; Fig. S1f). The fluorescence intensities of NMIIA, MLC, p-MLC and α-actinin were similar for all sectors of circular cells (Fig. S4). However, there was a significant reduction in the relative intensity of NMIIA, MLC and p-MLC, but not of α-actinin, near the vertices of square cells compared to flat-edge regions (30 °~60 ° vs. 0 °~30 ° and 60 °~90 ° sectors, see Fig. S4).

Since the orientation of F-actin was uniform in circular cells but varied with angular sector in square cells (Fig. 3d; Fig. S1e; Fig. S2c), we speculated that the association of F-actin with NMIIA, MLC, p-MLC, and α-actinin could also vary spatially. Thus, we computed the Pearson's correlation coefficients (PCs) of F-actin relative to NMIIA, MLC, p-MLC, and α-actinin across different angular sectors (Fig. 3f). This analysis showed that NMIIA, MLC, p-MLC, and α-actinin co-localized with F-actin at a similar level across all the sectors of the circular cells. In contrast, the association of NMIIA, MLC, and p-MLC with F-actin in square cells was reduced near the vertices when compared with that in the flat-edge regions (Fig. 3f; Fig. S1g). In square cells, the F-actin bundles were aligned perpendicular to the cell edge at the vertices (Fig. 3d; Fig. S1e), where NMIIA, MLC, and p-MLC were largely

absent (Fig. 3e–f; Fig. S1f–g). Our results imply a decreased association of NMIIA, MLC, and p-MLC with the radial F-actin bundles near the cell vertics. Thus, the actin-crosslinking protein α-actinin-1 [53] was localized within both the radial fibers and the transverse fibers, while NMIIA, MLC, and p-MLC were mainly associated with the transverse fibers (Fig. 3e–f; Fig. S1f–g; Fig. S4).

To confirm the effect of myosin-II-mediated contractility within the assembly of transverse fibers, we used the small-molecule inhibitors blebbistatin [54,55] and Y27632 [56] to inhibit myosin-II ATPase activity and Rho-associated kinase (ROCK)-mediated MLC phosphorylation, respectively. Inhibition of either myosin-II ATPase activity or MLC phosphorylation blocked the formation of transverse fibers and produced faded radial fibers (Fig. 3g). Therefore, our results suggest that NMIIA, MLC, and p-MLC are present in the transverse fibers (Fig. 3e–f; Fig. S1f–g; Fig. S4) in order to create the number of transverse arcs and generate actomyosin contractility [57–60] (Fig. 3g), whereas the radial fibers are connected with the peripheral FAs (Fig. 3a–d; Fig. S1e; Fig. S2c; Fig. S3).

To further examine the relative movement of the transverse fibers and the radial fibers in the circular and square MSCs, these cells were transfected with F-tractin-GFP (inositol 1,4,5-Trisphosphate 3-Kinase A N66 actin binding domain fused to GFP) [61], so that various patterns of F-actin could be examined via confocal microscopy. Based on time-lapse images, we observed the following in circular cells: (1) the thin actin bundles in the actin network were oriented parallel to the cell edge (transverse fibers) and moved centripetally in a counter-clockwise direction; (2) the radial fibers swirled toward cell center from the peripheral FAs (Video S1). In contrast, in the square cells, the concentrated bundles of radial fibers at the vertices established a symmetrical pattern that disrupted the counter-clockwise swirling to result in a centripetal movement that bridged the transverse fibers (Video S2). Thus, we speculated that the myosin II-mediated contractile force on the transverse fibers is transmitted along the radial fibers to the ECM through the FAs. To test this hypothesis, we measured the traction stresses generated by MSCs plated on the circular and square islands for 16 h under standard growth conditions. Fig. 4a shows the maps of the in-plane traction stress vector (i.e., tangential (t_{xz},t_{yz}), see Materials and Methods) overlaid on DIC images of the cells. In both circular and square cells, the in-plane traction stresses showed a contractile pattern pointing to-wards the cell center (Fig. 4a). The overall traction force was higher in the square cells than in the circular ones (Fig. 4b). Furthermore, while the traction stresses were uniformly distributed along the edge of the circular cells, they were concentrated near the corners in the square cells (Fig. 4c–d). In order to investigate how the traction stresses distribution, mediated by cell shape, affect the mechanical loads born by the cytoskeleton, we used monolayer stress microscopy to determine the intracellular tension and its orientation. Fig. S5a shows maps of the intracellular tension where the segments represent the direction of maximum tension (i.e., the principal direction of maximum intracellular stress, see Materials and Methods). This analysis revealed that intracellular tension was lower in the circular cells than in the square cells (Fig. S5b). Our analysis also indicated a trend for intracellular tension to concentrate at the vertices of the square cells as opposed to a uniform distribution in circular cells (Fig. S5c). The localization and the orientation of intracellular tension were similar to those of the radial fibers. Taken

together, these data suggest that the contractile forces generated at the transverse fibers are transmitted to FAs through the radial fibers.

3.4. Systematic coordination of integrin-mediated adhesions and actin polymerization maintains cell shape

Because the recognition of fibronectin by integrin $\alpha 5\,\beta 1$ and $\alpha v\,\beta 3$ has been well-defined [62], we determined whether integrin $\beta 1$ or $\beta 3$ activities affect FAs and the assembly of radial and transverse fibers. Using integrin $\beta 1$ and integrin $\beta 3$ function-blocking antibodies, fibronectin-mediated integrin $\beta 1$ and integrin $\beta 3$ activation could be inhibited, respectively. We first tested whether the regulation of cell spreading on the square islands was primarily influenced by integrin $\beta 1$ or $\beta 3$. A significant reduction in the cell spreading capability was detected when MSCs were treated with integrin $\beta 1$ function-blocking antibodies, but not in those treated with integrin $\beta 3$ function-blocking antibodies (Fig. S6a). For these well-spreading cells on the circular or square islands, we found that neither integrin $\beta 1$ nor integrin $\beta 3$ function-blocking antibodies affected the assembly of radial and transverse fibers; however, significant shortening of FA length was observed in the vertex sectors of square cells (Fig. S6b–c). We further speculated that the association of NMIIA with F-actin could be affected. Indeed, the reduced association of NMIIA with F-actin near the vertices of the square cells was disrupted by integrin $\beta 1$ or $\beta 3$ function-blocking antibodies (Fig. S6d–e). The images revealed the increased association of NMIIA with the radial F-actin bundles (Fig. S6d), implying that blockage of integrin $\beta 1$ or $\beta 3$ activities could interfere the spatial distribution of NMIIA, which may also affect the distribution of intracellular tension to limit FA maturation. Altogether, the results indicated that integrin $\beta 1$ could aid MSCs to spread on fibronectin-coated islands, and both integrin $\beta 1$ and $\beta 3$ activities could control the localization of NMIIA, which may also control the spatial distribution of intracellular tension, for FA maturation.

To further elucidate the role of cytoskeleton dynamics in maintaining cell shape guided by the underlying substrate, we used small-molecule inhibitors to block actin and microtubule polymerization. Inhibition of actin polymerization by latrunculin A or cytokalasin D led to the disassembly of the bundled actin filaments, the disappearance of the FAs, and the loss of cell attachment on both circular and square micropatterns (Fig. S7a). Disruption of microtubules by nocodazole did not block the formation of the actin filaments and FAs or cell spreading into the micropatterns, although it caused chyral patterns in the organization of the actin cytoskeleton and the orientation of the FAs (Fig. S7a). In addition, Immunolocalization of F-actin and the lamellipodia marker cortactin in MSCs revealed that lamellipodia were formed at the cell edge of both the circular and square cells (Fig. S7b). These data suggest that the enrichment of actin polymerization at the cell periphery could sustain cell spreading within the circular, as well as the square micropatterns.

3.5. Focusing of cellular contractile force modulates nuclear volume

In square-shaped MSCs, the intracellular tension increased and became concentrated along the square diagonals (Fig. 4a–d; Fig. S5), and MSC lineage determination was guided towards osteoblasts (Fig. 1). We sought to determine whether intracellular tension propagated to the cell nucleus resulting in cell-shape modulation of nuclear deformation.

We measured the out-of-plane traction stresses in the circular and the square cells (i.e., the normal component t_{zz}, see Materials and Methods) and mapped these stresses overlaid on DIC images (Fig. 4e). The maps indicate that the cells pulled upward and away from the substrate ($t_{zz} > 0$) along the same regions where they exerted in-plane traction stresses, consistent with previous studies [63]. Additionally, the out-of-plane stress maps reveal that the interior of the cells was pushed down against the substrate ($t_{zz} < 0$), implying that their nucleus was compressed. We determined the total compressive force (i.e., the surface sum of t_{zz} within $t_{zz} < 0$ regions), finding that the cell nucleus underwent significantly stronger compressive force in square cells than in circular cells (Fig. 4f). We further imaged the nucleus with confocal microscopy (Fig. 4g), and measured the nuclear projected area (Fig. 4h left), nuclear shape factor (the ratio of nuclear projection perimeter to that of a circle of equal area, Fig. 4h middle), and nuclear height (Fig. 4h right). The projected area and shape factor of nucleus in cells on the circular or square islands were similar. However, the square cells had a significantly lower nuclear height (~13%) than the circular cells. These results indicate that the increased actomyosin-generated intracellular tension in square cells flattened the cell nucleus and decreased its volume. We further examined the modulation of nuclear stiffness by cell shape via video particle tracking microrheology (VPTM) [49,64–68]. In this experiment, 200-nm diameter fluorescence beads were ballistically injected into MSCs using a biolistic particle delivery system [64,69] to disperse the beads throughout the nucleus. Subsequently, the cells were plated on circular and square micropatterns and imaged using high-resolution video-microscopy; this allowed tracking of the Brownian motion of the beads, which reflected the viscoelastic properties inside the nucleus of the MSCs. The results revealed that the elastic modulus (Pa) in the nucleus was significantly higher in square cells compared to circular cells (Fig. 4i), possibly due to increased intranuclear crowding caused by decreased nuclear volume.

These results led us to hypothesize that geometrical constraints regulated mechanoactive signaling via the Yes-associated protein (YAP)/transcriptional coactivator with PDZ-binding motif (TAZ), since YAP/TAZ have been identified as key mechanotransducers [70–72]. YAP localizes in both the cytoplasm and the nucleus, and YAP nuclear translocation was identified as an important factor for osteogenesis during bone remodeling [72]. To test this hypothesis, we determined whether cell shape elicited changes in YAP nuclear localization. We performed immunolocalization of YAP and DAPI (the latter to visualize the nucleus) in MSCs plated on circular and square micropatterns (Fig. 4j). The results showed that cells cultured on square islands had a significant increase in YAP nuclear localization compared with those cultured on circular islands (Fig. 4k). Thus, nuclear shape, nuclear mechanics, and nuclear deformability can be controlled by the underlying patterns of the adhesive surface via the spatial organization of the cellular contractile forces.

To further confirm whether the focusing of cytoskeletal forces regulated the nucleus via linkage between the actin cytoskeleton and the nuclear envelope, we examined nuclear deformability and YAP nuclear translocation in cells where the linkage between the cytoskeleton and the nucleus was disrupted. Specifically, we perturbed the Nesprin-2, a protein of linker of nucleoskeleton and cytoskeleton complex (LINC complex). Nesprin-2 localizes predominantly nearby the outer nuclear envelope and binds F-actin via its klarischt sequence (KASH domain) [73]. We overexpressed the GFP-Nesprin-2(N)-klarischt sequence

(GFP-KASH) [74], which is a dominant negative mutant of Nesprin-2 that disrupts the linkage between the actin cytoskeleton and the nuclear envelope. In control cells expressing GFP-C1, the height of the nuclei decreased in square cells compared with those in circular cells. The expression of GFP-KASH disrupted nuclear flattening in square cells (Fig. 4l). In addition, GFP-KASH expression inhibited YAP nuclear translocation in the square cells (Fig. 4m). Overall, these data suggest that mechanical load of polarized actin filaments on the nucleus plays an important role in mechanical sensing via specific pathways. Furthermore, we found that the level of nuclear mechanical load can be adjusted by focusing intracellular forces via geometrical pattering of the cell substrate.

To confirm the notion that the geometrically-controlled YAP nuclear translocation by focusing intracellular force enhances osteogenesis in the square cells, we used a series of small-molecule inhibitors to further examine the impact of disrupting geometry-driven intracellular tension and YAP nuclear translocation on MSC lineage commitment. First, we suppressed intracellular tension by treating the cells with blebbistatin [54,55] or Y27632 [56] to inhibit myosin-II ATPase activity or ROCK-mediated MLC phosphorylation, respectively. We found that, on square micropatterns, treatment of blebbistatin or Y27632 caused the lineage of square MSCs toward adipogenesis (Fig. 4n). We further confirmed this phenomenon by examining the expression of adipogenic transcription factor PPARγ [75] and osteogenic transcription factor Runx2 and DLX5 [76]. Indeed, we detected an increased expression of PPARγ (Fig. 4o) and decreased expressions of Runx2 (Fig. S8) and DLX5 (Fig. 4p) in the square cells treated with blebbistatin or Y27632. In addition, in order to disrupt the effect of YAP in nucleus, we used verteporfin [77] or peptide 17 [78] to enhance YAP cytoplasmic retention or to inhibit YAP-TEAD interaction, respectively. We found that, in square MSCs, treatment of verteporfin or peptide 17 strongly suppressed MSC commitment toward osteogenesis, leading to adipogenic differentiation (Fig. 4n). Treating the square cells with verteporfin or peptide 17 significantly enhanced the expression of PPARγ (Fig. 4o) and suppressed DLX5 expression (Fig. 4p). These results suggest that nuclear translocation of YAP could be modified by geometry-controlled intracellular force to dictate MSC commitment.

3.6. FAs control force transmission to the nucleus through polarized actin filaments

To explore the nuclear changes elicited by cell shape, we investigated whether FAs present in the vertices of the square cells play a crucial role in transmitting intracellular tension to the nucleus to regulate MSC differentiation. Using microcontact printing, we generated “arch” islands (10,000 μm^2; Fig. 5a) of fibronectin on the PDMS substrates, as shown in Fig. 1a. These arched islands contain rounded corners, which serve as an intermediate case between square islands (4 corners of 90°) and circle islands (no corners). Single MSCs were then cultured on the circular, arched, and square micropatterns, and probed using immunofluorescence to observe the FAs and F-actin (Fig. 5b). In arched cells, larger FAs were assembled at the 30 °~60 ° sector corresponding to the rounded corners, similar to the square islands (Fig. 5c–d). However, the lower curvature of the rounded corners in the arched islands caused a decrease in the FA length compared to the square islands (3.43 ± 0.12 μm vs. 7.01 ± 0.25 μm, Fig. 5d). Next, we examined the orientation of the paxillin-marked FAs and F-actin at the rounded corners of the arched islands; we found that

they were still preferentially perpendicular to the cell membrane, as opposed to the 0°~30° and 60°~90° sectors, corresponding to a flat cell border (Fig. 5e). However, rounding the vertices (30°~60°) disrupted the perfect alignment between the FAs and F-actin in the square cells (Fig. 5e). Thus, in the cells without symmetrical vertices, FAs are less able to mature and connect with bundled actin filaments.

Since the loss of sharp corners in the cell border disrupted the alignment of the FAs and the bundled actin filaments, we hypothesized that it could influence YAP nuclear translocation by redistributing the cellular contractile forces. Analysis of YAP nuclear translocation revealed that YAP importation was significantly lower in the arched cells than in the square cells (Fig. 5f). We also examined the effect of sharp vs. rounded cell edges on MSC lineage commitment. As shown in Fig. 1, MSCs plated on the square micropatterns showed a decrease in adipogenesis and an increase in osteogenesis. Such a lineage was disrupted in arched cells (Fig. 5g), indicating that the sharp corners in the square cells plays a crucial role in dictating MSC commitment toward osteogenesis.

4. Discussion

This work aimed to examine the mechanisms involved in the commitment of MSCs towards an osteogenic fate and, in particular, to determine how mechanically-stimulated FAs control this process. To achieve this goal, we plated MSCs onto adhesive islands with and without sharp corners (i.e., circular vs. square). Upon adhering and spreading on circular islands, cells preferentially adopted adipocyte lineage, whereas square islands led preferentially to osteogenesis. Thus, patterned surfaces can provide controlled experimental conditions to study the detailed mechanisms underlying MSC differentiation guided by mechanically-stimulated FAs. We found that adhesive patterns containing sharp corners promoted the formation of organized FAs, which further enhanced the alignment and polarization of the radial stress fibers. These fibers re-distributed transverse fibers contractility and transduced intracellular tension to the cell nucleus. The tauter cytoskeletal network pressed the cell nucleus against the substrate and increased nuclear translocation of the transcription co-activator YAP, which in turn promoted MSC osteogenic differentiation (Fig. 6). *Pan et al.* [72] have determined the essential role of YAP nuclear translocation in maintaining nuclear β-catenin level to proceed Wnt/β-catenin signaling for MSC osteogenesis, supporting our hypothesis that the interaction between nuclear YAP and TEA domain (TEAD) containing family transcriptional factors is a crucial step for osteogenesis. Indeed, either disrupting YAP nuclear translocation by using verteporfin to retain YAP in cytoplasm or suppressing YAP-TEAD interaction by using peptide 17 significantly suppressed osteogenesis of MSCs in square cells. These findings bring to light the crucial role of FAs in sensing geometric cues to further establish the dynamic cytoskeletal network, which focuses the intracellular tension towards the nucleus to control YAP mechanotransduction signaling for MSC fate determination.

The YAP/TAZ mechanotransduction pathway mediates MSC mechanosensing [70–72]. Several studies have revealed that YAP can be controlled by various biochemical and mechanical cues. At the biochemical level, the Hippo signaling pathway regulates YAP/TAZ activity [79]. Within the Hippo kinase cascade, Ste20-like kinases 1/2

(MST1/2) phosphorylates and activates large tumor suppressor 1/2 (LATS1/2), which then phosphorylates YAP/TAZ and restricts nuclear import and activation [79]. At the mechanical level, YAP is regulated by ECM rigidity, strain, shear stress, and adhesive area [71,80–85]. These mechanical stimuli require cytoskeletal integrity, RhoA GTPase activity, and myosin-II-mediated contractility, but are independent of the Hippo/LATS cascade. We determined that the mechanical connection between the nucleus and the cytoskeleton allows force to be transmitted to the nucleus, leading to nuclear flattening and YAP nuclear import. Although regulation of YAP has been investigated previously, our study has revealed a novel mechanism whereby FAs control YAP nuclear translocation by focusing intracellular tension towards the nucleus. This new finding indicates that FAs play a crucial role in mechanosensing by controlling the contractile architecture of the cytoskeleton.

In previous studies, the cell shape was modulated via patterned substrate to study cytoskeleton dynamics [57,86–89], cell motility [90–92], and MSC fate decisions [5,20,22] with single-cell resolution. These studies have shown that cell size and cell shape strongly influence MSC differentiation by modulating actomyosin contractility [5,20]. *Kilian et al* [20] have shown that ERK/JNK signaling cascade serves as the downstream signals of the tension-specific loop between actin cytoskeleton and FAs to tune the switch between osteogenesis and adipogenesis. However, there remains a lack of a comprehensive investigation on how different cell shapes manipulate cytoskeletal network to control tension-specific loop, and to further correlate with nuclear signals for MSC differentiation. We demonstrated that FAs play a crucial role in sensing geometric cues and, in particular, that the existence of high-curvature regions in the cellular shape guides their maturation process. FAs concentrate the spatial distribution of intracellular tension generated by transverse fibers through bundling the radial stress fibers, and thereby providing the cell with a force to deform the nucleus during mechanotransduction. This mechanism was demonstrated by two series of experiments. First, we removed high-curvature cell shape regions by replacing sharp corners with smooth arches in the substrate micropatterns, which limited FA growth and restrained the alignment between FAs and radial fibers. Next, we used a dominant negative mutant of Nesprin-2, KASH sequence [74], to disconnect the nucleus-cytoskeleton interface [93] and impair YAP nuclear translocation in square cells. In both arched cells and KASH-expressing square cells, disrupting the mechanical coupling between FAs and the nuclear envelope caused a reduction in the nuclear translocation of YAP, and weakened MSC commitment towards the osteoblast lineage. Altogether, we conclude that the FAs respond to geometric cue to establish FA-nuclear mechanical coupling by modulating the contractility and spatial organization of different domains (i.e., the radial and transverse fibers) in the actin cytoskeleton, and this translates the physical signals from geometric features into biological activities that control MSC fate commitment.

Within heterogeneous architecture of tissues, cell shape guided by ECM geometry can determine stem cell fate, and our findings have shown that FAs are crucial to sense and respond to geometric cues. The consequential modulation of the size and protein compositions of FAs, through their connection to actin filaments, can control actin orientation and guide the distribution of cellular contractile forces. Of note, FAs regulate the nuclear-actomyosin force balance for YAP mechanotransduction and subsequently, the differentiation process of MSCs. Therefore, FAs play a pivotal role in controlling the

orientation and distribution of actin filaments, as well as the linkage between the actin cytoskeleton and the nuclear envelope; these in turn control transcriptional regulation during MSC differentiation.

5. Conclusion

In response to extracellular geometric features, MSCs spread via the formation of cellular adhesive organelles, FAs, which connect with the radial stress fibers to bridge with the transverse fibers, and to establish the dynamic cytoskeletal network. In the high-curvature cell shape regions, FAs responded to the physical constraint by changing their protein composition to become mature. Mature FAs act as the starting points to enhance the clustering of the symmetrical radial fiber bundles that concentrate the contractile force generated by the transverse fibers. The concentrated contractile force transmits along the clustered radial fiber bundles inward to control nuclear-actomyosin force balance, causing nuclear deformability by pressing down the nucleus. This cytoskeletal machinery controls the nuclear translocation of YAP, and in turn modulates the switch in MSC commitment towards osteogenesis.

Supplementary Material

Refer to Web version on PubMed Central for supplementary material.

Acknowledgements

This work is financially supported by the National Science and Technology Council, the Veterans General Hospitals and University System of Taiwan Joint Research Program, and the “Cancer Progression Research Center, National Yang Ming Chiao Tung University” from The Featured Areas Research Center Program within the framework of the Higher Education Sprout Project by the Ministry of Education (MOE) in Taiwan. The authors would like to acknowledge Prof. Catherine M. Shanahan laboratory (University of Cambrisge, UK) for providing the construct GFP-Nesprin-2 (ΔN)-klarischt sequence (GFP-KASH), and Prof. Ming-Wei Lin (National Yang Ming Chiao Tung University, Taiwan) for supporting the statistical analysis.

Funding

This work is jointly supported by research grants from the National Science and Technology Council (MOST 109–2326-B-010–002-MY3), from the Veterans General Hospitals and University System of Taiwan Joint Research Program (VGHUST110-G7–6-1), and from the Cancer Progression Research Center (National Yang Ming Chiao Tung University) from The Featured Areas Research Center Program within the framework of the Higher Education Sprout Project by the Ministry of Education (MOE) in Taiwan.

Abbreviations:

MSC	mesenchymal stromal cells
FA	focal adhesions
NMIIA	non-muscle myosin-II heavy chain-A
YAP	Yes-associated protein
TAZ	transcriptional coactivator with PDZ-binding motif

References

[1]. Deng J, Petersen BE, Steindler DA, Jorgensen ML, Laywell ED, Mesenchymal stem cells spontaneously express neural proteins in culture and are neurogenic after transplantation, Stem Cells 24 (4) (2006) 1054–1064. [PubMed: 16322639]

[2]. Hofstetter CP, Schwarz EJ, Hess D, Widenfalk J, El Manira A, Prockop DJ, Olson L, Marrow stromal cells form guiding strands in the injured spinal cord and promote recovery, Proc. Natl. Acad. Sci. USA 99 (4) (2002) 2199–2204. [PubMed: 11854516]

[3]. Horwitz EM, Le Blanc K, Dominici M, Mueller I, Slaper-Cortenbach I, Marini FC, Deans RJ, Krause DS, Keating A, International T Society for Cellular, Clarification of the nomenclature for MSC: the International Society for Cellular Therapy position statement, Cytotherapy 7 (5) (2005) 393–395. [PubMed: 16236628]

[4]. Kondo T, Johnson SA, Yoder MC, Romand R, Hashino E, Sonic hedgehog and retinoic acid synergistically promote sensory fate specification from bone marrow-derived pluripotent stem cells, Proc. Natl. Acad. Sci. USA 102 (13) (2005) 4789–4794. [PubMed: 15778294]

[5]. McBeath R, Pirone DM, Nelson CM, Bhadriraju K, Chen CS, Cell shape, cytoskeletal tension, and RhoA regulate stem cell lineage commitment, Dev. Cell 6 (4) (2004) 483–495. [PubMed: 15068789]

[6]. Pittenger MF, Mackay AM, Beck SC, Jaiswal RK, Douglas R, Mosca JD, Moorman MA, Simonetti DW, Craig S, Marshak DR, Multilineage potential of adult human mesenchymal stem cells, Science 284 (5411) (1999) 143–147. [PubMed: 10102814]

[7]. Uccelli A, Moretta L, Pistoia V, Mesenchymal stem cells in health and disease, Nat. Rev. Immunol. 8 (9) (2008) 726–736. [PubMed: 19172693]

[8]. Valtieri M, Sorrentino A, The mesenchymal stromal cell contribution to homeostasis, J. Cell. Physiol. 217 (2) (2008) 296–300. [PubMed: 18615579]

[9]. Krampera M, Le Blanc K, Mesenchymal stromal cells: Putative microenvironmental modulators become cell therapy, Cell Stem Cell 28 (10) (2021) 1708–1725. [PubMed: 34624232]

[10]. Brooke G, Cook M, Blair C, Han R, Heazlewood C, Jones B, Kambouris M, Kollar K, McTaggart S, Pelekanos R, Rice A, Rossetti T, Atkinson K, Therapeutic applications of mesenchymal stromal cells, Semin. Cell Dev. Biol. 18 (6) (2007) 846–858. [PubMed: 18024097]

[11]. Li CJ, Cheng P, Liang MK, Chen YS, Lu Q, Wang JY, Xia ZY, Zhou HD, Cao X, Xie H, Liao EY, Luo XH, MicroRNA-188 regulates age-related switch between osteoblast and adipocyte differentiation, J. Clin. Invest. 125 (4) (2015) 1509–1522. [PubMed: 25751060]

[12]. Hu L, Yin C, Zhao F, Ali A, Ma J, Qian A, Mesenchymal stem cells: cell fate decision to osteoblast or adipocyte and application in osteoporosis treatment, Int. J. Mol. Sci. 19 (2) (2018).

[13]. Moerman EJ, Teng K, Lipschitz DA, Lecka-Czernik B, Aging activates adipogenic and suppresses osteogenic programs in mesenchymal marrow stroma/stem cells: the role of PPAR-gamma2 transcription factor and TGF–beta/BMP signaling pathways, Aging Cell 3 (6) (2004) 379–389. [PubMed: 15569355]

[14]. Rodan GA, Harada S, The missing bone, Cell 89 (5) (1997) 677–680. [PubMed: 9182754]

[15]. Connelly JT, Garcia AJ, Levenston ME, Interactions between integrin ligand density and cytoskeletal integrity regulate BMSC chondrogenesis, J. Cell. Physiol. 217 (1) (2008) 145–154. [PubMed: 18452154]

[16]. Le Saux G, Wu MC, Toledo E, Chen YQ, Fan YJ, Kuo JC, Schvartzman M, Cell-cell adhesion-driven contact guidance and its effect on human mesenchymal stem cell differentiation, ACS Appl. Mater. Interfaces 12 (20) (2020) 22399–22409. [PubMed: 32323968]

[17]. Engler AJ, Sen S, Sweeney HL, Discher DE, Matrix elasticity directs stem cell lineage specification, Cell 126 (4) (2006) 677–689. [PubMed: 16923388]

[18]. Ward DF Jr., Salasznyk RM, Klees RF, Backiel J, Agius P, Bennett K, Boskey A, Plopper GE, Mechanical strain enhances extracellular matrix-induced gene focusing and promotes osteogenic differentiation of human mesenchymal stem cells through an extracellular-related kinase-dependent pathway, Stem Cells Dev. 16 (3) (2007) 467–480. [PubMed: 17610377]

[19]. Oh S, Brammer KS, Li YS, Teng D, Engler AJ, Chien S, Jin S, Stem cell fate dictated solely by altered nanotube dimension, Proc. Natl. Acad. Sci. USA 106 (7) (2009) 2130–2135. [PubMed: 19179282]

[20]. Kilian KA, Bugarija B, Lahn BT, Mrksich M, Geometric cues for directing the differentiation of mesenchymal stem cells, Proc. Natl. Acad. Sci. USA 107 (11) (2010) 4872–4877. [PubMed: 20194780]

[21]. Lee J, Abdeen AA, Huang TH, Kilian KA, Controlling cell geometry on substrates of variable stiffness can tune the degree of osteogenesis in human mesenchymal stem cells, J. Mech. Behav. Biomed. Mater. 38 (2014) 209–218. [PubMed: 24556045]

[22]. Lee J, Abdeen AA, Zhang D, Kilian KA, Directing stem cell fate on hydrogel substrates by controlling cell geometry, matrix mechanics and adhesion ligand composition, Biomaterials 34 (33) (2013) 8140–8148. [PubMed: 23932245]

[23]. Yang Y, Wang X, Wang Y, Hu X, Kawazoe N, Yang Y, Chen G, Influence of cell spreading area on the osteogenic commitment and phenotype maintenance of mesenchymal stem cells, Sci. Rep. 9 (1) (2019) 6891. [PubMed: 31053728]

[24]. Jockusch BM, Bubeck P, Giehl K, Kroemker M, Moschner J, Rothkegel M, Rudiger M, Schluter K, Stanke G, Winkler J, The molecular architecture of focal adhesions, Annu. Rev. Cell Dev. Biol. 11 (1995) 379–416. [PubMed: 8689563]

[25]. Hynes RO, The extracellular matrix: not just pretty fibrils, Science 326 (5957) (2009) 1216–1219. [PubMed: 19965464]

[26]. Hynes RO, Integrins: bidirectional, allosteric signaling machines, Cell 110 (6) (2002) 673–687. [PubMed: 12297042]

[27]. Burridge K, Fath K, Kelly T, Nuckolls G, Turner C, Focal adhesions: transmembrane junctions between the extracellular matrix and the cytoskeleton, Annu. Rev. Cell Biol. 4 (1988) 487–525. [PubMed: 3058164]

[28]. Schwartz MA, Schaller MD, Ginsberg MH, Integrins: emerging paradigms of signal transduction, Annu. Rev. Cell Dev. Biol. 11 (1995) 549–599. [PubMed: 8689569]

[29]. Zaidel-Bar R, Geiger B, The switchable integrin adhesome, J. Cell Sci. 123 (Pt 9) (2010) 1385–1388. [PubMed: 20410370]

[30]. Zaidel-Bar R, Itzkovitz S, Ma'ayan A, Iyengar R, Geiger B, Functional atlas of the integrin adhesome, Nat. Cell Biol. 9 (8) (2007) 858–867. [PubMed: 17671451]

[31]. Chrzanowska-Wodnicka M, Burridge K, Rho-stimulated contractility drives the formation of stress fibers and focal adhesions, J. Cell Biol. 133 (6) (1996) 1403–1415. [PubMed: 8682874]

[32]. Kuo JC, Mechanotransduction at focal adhesions: integrating cytoskeletal mechanics in migrating cells, J. Cell. Mol. Med. 17 (6) (2013) 704–712. [PubMed: 23551528]

[33]. Kuo JC, Han X, Hsiao CT, Yates JR 3rd, Waterman CM, Analysis of the myosin-II-responsive focal adhesion proteome reveals a role for beta-Pix in negative regulation of focal adhesion maturation, Nat. Cell Biol. 13 (4) (2011) 383–393. [PubMed: 21423176]

[34]. Pletjushkina OJ, Belkin AM, Ivanova OJ, Oliver T, Vasiliev JM, Jacobson K, Maturation of cell-substratum focal adhesions induced by depolymerization of microtubules is mediated by increased cortical tension, Cell Adhes. Commun. 5 (2) (1998) 121–135. [PubMed: 9638333]

[35]. Riveline D, Zamir E, Balaban NQ, Schwarz US, Ishizaki T, Narumiya S, Kam Z, Geiger B, Bershadsky AD, Focal contacts as mechanosensors: externally applied local mechanical force induces growth of focal contacts by an mDia1-dependent and ROCK-independent mechanism, J. Cell Biol. 153 (6) (2001) 1175–1186. [PubMed: 11402062]

[36]. Kuo JC, Focal adhesions function as a mechanosensor, Prog. Mol. Biol. Transl. Sci. 126 (2014) 55–73. [PubMed: 25081614]

[37]. Huang IH, Hsiao CT, Wu JC, Shen RF, Liu CY, Wang YK, Chen YC, Huang CM, del Alamo JC, Chang ZF, Tang MJ, Khoo KH, Kuo JC, GEF-H1 controls focal adhesion signaling that regulates mesenchymal stem cell lineage commitment, J. Cell Sci. 127 (Pt 19) (2014) 4186–4200. [PubMed: 25107365]

[38]. Yu YL, Chou RH, Chen LT, Shyu WC, Hsieh SC, Wu CS, Zeng HJ, Yeh SP, Yang DM, Hung SC, Hung MC, EZH2 regulates neuronal differentiation of mesenchymal stem cells through

PIP5K1C-dependent calcium signaling, J. Biol. Chem. 286 (11) (2011) 9657–9667. [PubMed: 21216957]

[39]. Ruiz SA, Chen CS, Microcontact printing: a tool to pattern, Soft Matter 3 (2) (2007) 11.

[40]. Vignaud T, Ennomani H, Thery M, Polyacrylamide hydrogel micropatterning, Methods Cell Biol. 120 (2014) 93–116. [PubMed: 24484659]

[41]. Wang YL, Pelham RJ Jr., Preparation of a flexible, porous polyacrylamide substrate for mechanical studies of cultured cells, Methods Enzymol. 298 (1998) 489–496. [PubMed: 9751904]

[42]. Del Alamo JC, Meili R, Alonso-Latorre B, Rodriguez-Rodriguez J, Aliseda A, Firtel RA, Lasheras JC, Spatio-temporal analysis of eukaryotic cell motility by improved force cytometry, Proc. Natl. Acad. Sci. USA 104 (33) (2007) 13343–13348. [PubMed: 17684097]

[43]. del Alamo JC, Meili R, Alvarez-Gonzalez B, Alonso-Latorre B, Bastounis E, Firtel R, Lasheras JC, Three-dimensional quantification of cellular traction forces and mechanosensing of thin substrata by fourier traction force microscopy, PLoS One 8 (9) (2013) e69850. [PubMed: 24023712]

[44]. Serrano R, Aung A, Yeh YT, Varghese S, Lasheras JC, Del Alamo JC, Three--dimensional monolayer stress microscopy, Biophys. J. 117 (1) (2019) 111–128. [PubMed: 31103228]

[45]. Tambe DT, Croutelle U, Trepat X, Park CY, Kim JH, Millet E, Butler JP, Fredberg JJ, Monolayer stress microscopy: limitations, artifacts, and accuracy of recovered intercellular stresses, PLoS One 8 (2) (2013) e55172. [PubMed: 23468843]

[46]. Chen YQ, Liu YS, Liu YA, Wu YC, Del Alamo JC, Chiou A, Lee OK, Biochemical and physical characterizations of mesenchymal stromal cells along the time course of directed differentiation, Sci. Rep. 6 (2016) 31547. [PubMed: 27526936]

[47]. Tseng Y, Lee JS, Kole TP, Jiang I, Wirtz D, Micro-organization and visco-e-lasticity of the interphase nucleus revealed by particle nanotracking, J. Cell Sci. 117 (Pt 10) (2004) 2159–2167. [PubMed: 15090601]

[48]. Chen Y-Q, Kuo C-Y, Wei M-T, Wu K, Su P-T, Huang C-S, Chiou A, Intra-cellular viscoelasticity of HeLa cells during cell division studied by video particle-tracking microrheology, J. Biomed. Opt. 19 (1) (2014) 011008–011008. [PubMed: 23864037]

[49]. Hale CM, Sun SX, Wirtz D, Resolving the role of actoymyosin contractility in cell microrheology, PLoS One 4 (9) (2009) e7054. [PubMed: 19756147]

[50]. Hernandez-Mosqueira C, Velez-delValle C, Kuri-Harcuch W, Tissue alkaline phosphatase is involved in lipid metabolism and gene expression and secretion of adipokines in adipocytes, Biochim. Biophys. Acta 1850 (12) (2015) 2485–2496. [PubMed: 26391843]

[51]. Kanchanawong P, Shtengel G, Pasapera AM, Ramko EB, Davidson MW, Hess HF, Waterman CM, Nanoscale architecture of integrin-based cell adhesions, Nature 468 (7323) (2010) 580–584. [PubMed: 21107430]

[52]. Pasapera AM, Schneider IC, Rericha E, Schlaepfer DD, Waterman CM, Myosin II activity regulates vinculin recruitment to focal adhesions through FAK-mediated paxillin phosphorylation, J. Cell Biol. 188 (6) (2010) 877–890. [PubMed: 20308429]

[53]. Sjoblom B, Salmazo A, Djinovic-Carugo K, Alpha-actinin structure and regulation, Cell. Mol. Life Sci. 65 (17) (2008) 2688–2701. [PubMed: 18488141]

[54]. Straight AF, Cheung A, Limouze J, Chen I, Westwood NJ, Sellers JR, Mitchison TJ, Dissecting temporal and spatial control of cytokinesis with a myosin II inhibitor, Science 299 (5613) (2003) 1743–1747. [PubMed: 12637748]

[55]. Roman BI, Verhasselt S, Stevens CV, Medicinal chemistry and use of myosin II inhibitor (S)-blebbistatin and its derivatives, J. Med. Chem. 61 (21) (2018) 9410–9428. [PubMed: 29878759]

[56]. Uehata M, Ishizaki T, Satoh H, Ono T, Kawahara T, Morishita T, Tamakawa H, Yamagami K, Inui J, Maekawa M, Narumiya S, Calcium sensitization of smooth muscle mediated by a Rho-associated protein kinase in hypertension, Nature 389 (6654) (1997) 990–994. [PubMed: 9353125]

[57]. Tee YH, Shemesh T, Thiagarajan V, Hariadi RF, Anderson KL, Page C, Volkmann N, Hanein D, Sivaramakrishnan S, Kozlov MM, Bershadsky AD, Cellular chirality arising from the

self-organization of the actin cytoskeleton, Nat. Cell Biol. 17 (4) (2015) 445–457. [PubMed: 25799062]

[58]. Hotulainen P, Lappalainen P, Stress fibers are generated by two distinct actin assembly mechanisms in motile cells, J. Cell Biol. 173 (3) (2006) 383–394. [PubMed: 16651381]

[59]. Tojkander S, Gateva G, Schevzov G, Hotulainen P, Naumanen P, Martin C, Gunning PW, Lappalainen P, A molecular pathway for myosin II recruitment to stress fibers, Curr. Biol. 21 (7) (2011) 539–550. [PubMed: 21458264]

[60]. Burnette DT, Manley S, Sengupta P, Sougrat R, Davidson MW, Kachar B, Lippincott-Schwartz J, A role for actin arcs in the leading-edge advance of migrating cells, Nat. Cell Biol. 13 (4) (2011) 371–381. [PubMed: 21423177]

[61]. Schell MJ, Erneux C, Irvine RF, Inositol 1,4,5-trisphosphate 3-kinase A associates with F-actin and dendritic spines via its N terminus, J. Biol. Chem. 276 (40) (2001) 37537–37546. [PubMed: 11468283]

[62]. Danen EH, Sonneveld P, Brakebusch C, Fassler R, Sonnenberg A, The fibronectin-binding integrins alpha5beta1 and alphavbeta3 differentially modulate RhoA-GTP loading, organization of cell matrix adhesions, and fibronectin fibrillogenesis, J. Cell Biol. 159 (6) (2002) 1071–1086. [PubMed: 12486108]

[63]. Hur SS, Zhao Y, Li YS, Botvinick E, Chien S, Live cells exert 3-dimensional traction forces on their substrata, Cell. Mol. Bioeng. 2 (3) (2009) 425–436. [PubMed: 19779633]

[64]. Chen YQ, Kuo CY, Wei MT, Wu K, Su PT, Huang CS, Chiou A, Intracellular viscoelasticity of HeLa cells during cell division studied by video particle-tracking microrheology, J. Biomed. Opt. 19 (1) (2014) 011008. [PubMed: 23864037]

[65]. del Alamo JC, Norwich GN, Li YS, Lasheras JC, Chien S, Anisotropic rheology and directional mechanotransduction in vascular endothelial cells, Proc. Natl. Acad. Sci. USA 105 (40) (2008) 15411–15416. [PubMed: 18840694]

[66]. Hur SS, del Alamo JC, Park JS, Li YS, Nguyen HA, Teng D, Wang KC, Flores L, Alonso-Latorre B, Lasheras JC, Chien S, Roles of cell confluency and fluid shear in 3-dimensional intracellular forces in endothelial cells, Proc. Natl. Acad. Sci. USA 109 (28) (2012) 11110–11115. [PubMed: 22665785]

[67]. Panorchan P, Lee JS, Kole TP, Tseng Y, Wirtz D, Microrheology and ROCK signaling of human endothelial cells embedded in a 3D matrix, Biophys. J. 91 (9) (2006) 3499–3507. [PubMed: 16891369]

[68]. Wirtz D, Particle-tracking microrheology of living cells: principles and applications, Annu. Rev. Biophys. 38 (2009) 301–326. [PubMed: 19416071]

[69]. Wu PH, Hale CM, Chen WC, Lee JS, Tseng Y, Wirtz D, High-throughput ballistic injection nanorheology to measure cell mechanics, Nat. Protoc. 7 (1) (2012) 155–170. [PubMed: 22222790]

[70]. Cai X, Wang KC, Meng Z, Mechanoregulation of YAP and TAZ in cellular homeostasis and disease progression, Front. Cell Dev. Biol. 9 (2021) 673599. [PubMed: 34109179]

[71]. Dupont S, Morsut L, Aragona M, Enzo E, Giulitti S, Cordenonsi M, Zanconato F, Le Digabel J, Forcato M, Bicciato S, Elvassore N, Piccolo S, Role of YAP/TAZ in mechanotransduction, Nature 474 (7350) (2011) 179–183. [PubMed: 21654799]

[72]. Pan JX, Xiong L, Zhao K, Zeng P, Wang B, Tang FL, Sun D, Guo HH, Yang X, Cui S, Xia WF, Mei L, Xiong WC, YAP promotes osteogenesis and suppresses adipogenic differentiation by regulating beta-catenin signaling, Bone Res. 6 (2018) 18. [PubMed: 29872550]

[73]. Zhang Q, Ragnauth CD, Skepper JN, Worth NF, Warren DT, Roberts RG, Weissberg PL, Ellis JA, Shanahan CM, Nesprin-2 is a multi-isomeric protein that binds lamin and emerin at the nuclear envelope and forms a subcellular network in skeletal muscle, J. Cell Sci. 118 (Pt 4) (2005) 673–687. [PubMed: 15671068]

[74]. Zhang Q, Skepper JN, Yang F, Davies JD, Hegyi L, Roberts RG, Weissberg PL, Ellis JA, Shanahan CM, Nesprins: a novel family of spectrin-repeat-containing proteins that localize to the nuclear membrane in multiple tissues, J. Cell Sci. 114 (Pt 24) (2001) 4485–4498. [PubMed: 11792814]

[75]. Lee JE, Ge K, Transcriptional and epigenetic regulation of PPARgamma expression during adipogenesis, Cell Biosci. 4 (2014) 29. [PubMed: 24904744]

[76]. Samee N, Geoffroy V, Marty C, Schiltz C, Vieux-Rochas M, Levi G, de Vernejoul MC, Dlx5, a positive regulator of osteoblastogenesis, is essential for osteoblast-osteoclast coupling, Am. J. Pathol. 173 (3) (2008) 773–780. [PubMed: 18669617]

[77]. Feng J, Gou J, Jia J, Yi T, Cui T, Li Z, Verteporfin, a suppressor of YAP-TEAD complex, presents promising antitumor properties on ovarian cancer, Onco. Targets Ther. 9 (2016) 5371–5381. [PubMed: 27621651]

[78]. Zhang Z, Lin Z, Zhou Z, Shen HC, Yan SF, Mayweg AV, Xu Z, Qin N, Wong JC, Zhang Z, Rong Y, Fry DC, Hu T, Structure-based design and synthesis of potent cyclic peptides inhibiting the YAP-TEAD protein-protein interaction, ACS Med. Chem. Lett. 5 (9) (2014) 993–998. [PubMed: 25221655]

[79]. Meng Z, Moroishi T, Guan KL, Mechanisms of Hippo pathway regulation, Genes Dev. 30 (1) (2016) 1–17. [PubMed: 26728553]

[80]. Wada K, Itoga K, Okano T, Yonemura S, Sasaki H, Hippo pathway regulation by cell morphology and stress fibers, Development 138 (18) (2011) 3907–3914. [PubMed: 21831922]

[81]. Nakajima H, Yamamoto K, Agarwala S, Terai K, Fukui H, Fukuhara S, Ando K, Miyazaki T, Yokota Y, Schmelzer E, Belting HG, Affolter M, Lecaudey V, Mochizuki N, Flow-dependent endothelial YAP regulation contributes to vessel maintenance, Dev. Cell 40 (6) (2017) 523–536 e6. [PubMed: 28350986]

[82]. Elosegui-Artola A, Oria R, Chen Y, Kosmalska A, Perez-Gonzalez C, Castro N, Zhu C, Trepat X, Roca-Cusachs P, Mechanical regulation of a molecular clutch defines force transmission and transduction in response to matrix rigidity, Nat. Cell Biol. 18 (5) (2016) 540–548. [PubMed: 27065098]

[83]. Calvo F, Ege N, Grande-Garcia A, Hooper S, Jenkins RP, Chaudhry SI, Harrington K, Williamson P, Moeendarbary E, Charras G, Sahai E, Mechanotrans-duction and YAP-dependent matrix remodelling is required for the generation and maintenance of cancer-associated fibroblasts, Nat. Cell Biol. 15 (6) (2013) 637–646. [PubMed: 23708000]

[84]. Benham-Pyle BW, Pruitt BL, Nelson WJ, Cell adhesion. Mechanical strain induces E-cadherin-dependent Yap1 and beta-catenin activation to drive cell cycle entry, Science 348 (6238) (2015) 1024–1027. [PubMed: 26023140]

[85]. Aragona M, Panciera T, Manfrin A, Giulitti S, Michielin F, Elvassore N, Dupont S, Piccolo S, A mechanical checkpoint controls multicellular growth through YAP/TAZ regulation by actin-processing factors, Cell 154 (5) (2013) 1047–1059. [PubMed: 23954413]

[86]. James J, Goluch ED, Hu H, Liu C, Mrksich M, Subcellular curvature at the perimeter of micropatterned cells influences lamellipodial distribution and cell polarity, Cell Motil. Cytoskeleton 65 (11) (2008) 841–852. [PubMed: 18677773]

[87]. Chen CS, Alonso JL, Ostuni E, Whitesides GM, Ingber DE, Cell shape provides global control of focal adhesion assembly, Biochem. Biophys. Res. Commun. 307 (2) (2003) 355–361. [PubMed: 12859964]

[88]. Parker KK, Tan J, Chen CS, Tung L, Myofibrillar architecture in engineered cardiac myocytes, Circ. Res. 103 (4) (2008) 340–342. [PubMed: 18635822]

[89]. Thery M, Pepin A, Dressaire E, Chen Y, Bornens M, Cell distribution of stress fibres in response to the geometry of the adhesive environment, Cell Motil. Cytoskeleton 63 (6) (2006) 341–355. [PubMed: 16550544]

[90]. Jiang X, Bruzewicz DA, Wong AP, Piel M, Whitesides GM, Directing cell migration with asymmetric micropatterns, Proc. Natl. Acad. Sci. USA 102 (4) (2005) 975–978. [PubMed: 15653772]

[91]. Parker KK, Brock AL, Brangwynne C, Mannix RJ, Wang N, Ostuni E, Geisse NA, Adams JC, Whitesides GM, Ingber DE, Directional control of lamellipodia extension by constraining cell shape and orienting cell tractional forces, FASEB J. 16 (10) (2002) 1195–1204. [PubMed: 12153987]

[92]. Brock A, Chang E, Ho CC, LeDuc P, Jiang X, Whitesides GM, Ingber DE, Geometric determinants of directional cell motility revealed using microcontact printing, Langmuir 19 (5) (2003) 1611–1617. [PubMed: 14674434]

[93]. Crisp M, Liu Q, Roux K, Rattner JB, Shanahan C, Burke B, Stahl PD, Hodzic D, Coupling of the nucleus and cytoplasm: role of the LINC complex, J. Cell Biol. 172 (1) (2006) 41–53. [PubMed: 16380439]

Statement of Significance

We decipher how cellular mechanics is self-organized depending on extracellular geometric features to correlate with mesenchymal stromal cell lineage commitment. In response to geometry constrains on cell morphology, symmetrical radial fiber bundles are assembled and clustered depending on the maturation state of focal adhesions and bridge with the transverse fibers, and thereby establishing the dynamic cytoskeletal network. Contractile force, generated by the myosin-IIA-enriched transverse fibers, is transmitted and dynamically drives the retrograde movement of the actin cytoskeletal network, which appropriately adjusts the nuclear-actomyosin force balance and deforms the cell nucleus for YAP mechanotransduction signaling in regulating mesenchymal stromal cell fate decision.

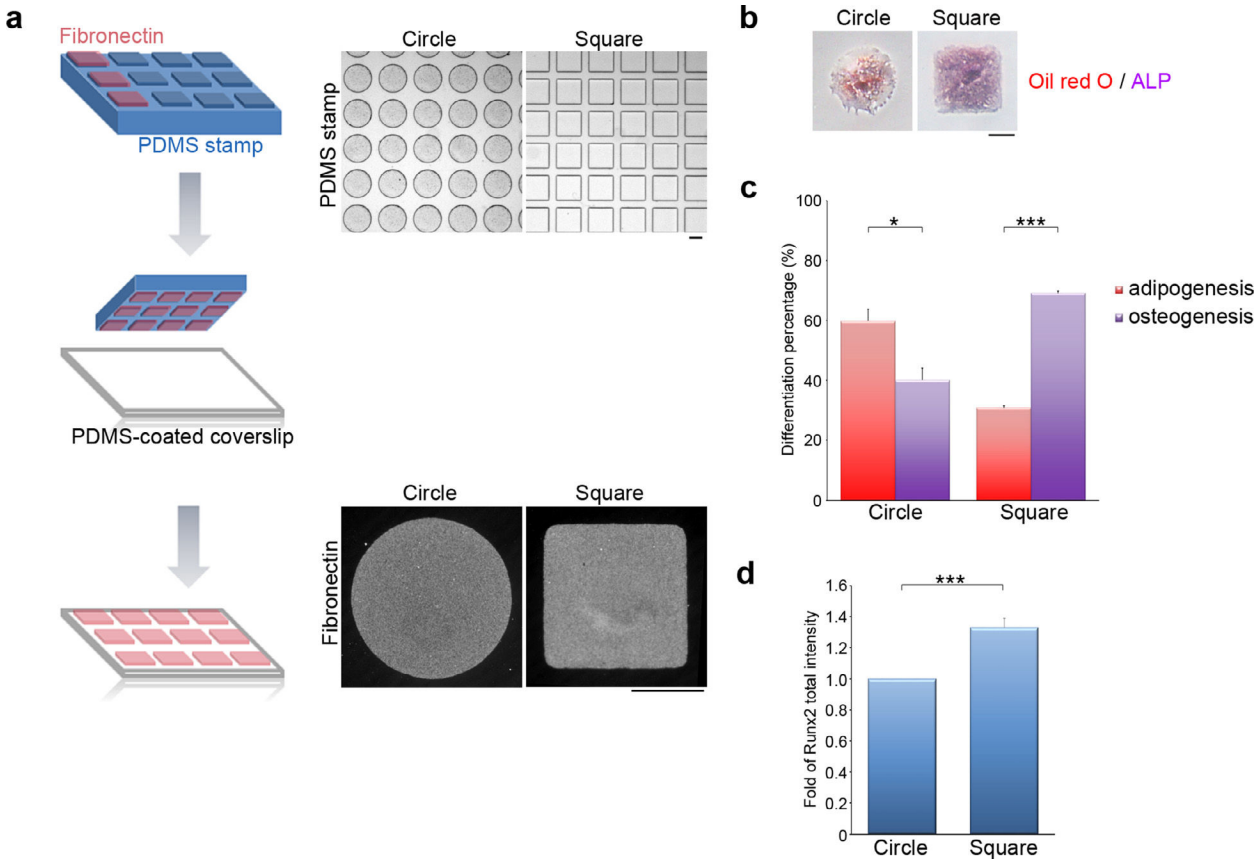

Fig. 1. MSC osteogenesis vs. adipogenesis depends on cell geometry.

(a) Left: A schematic illustration of the microcontact printing method used to control cell shape. Up-right: A polydimethylsiloxane (PDMS) stamp with micron-sized features, shown as phase images, was coated with fibronectin (50 μg/ml). The fibronectin was transferred from the raised features on the stamp onto a PDMS-coated glass coverslip via micro-contact printing. The gaps between fibronectin islands were blocked using Pluronic F127 to prevent cell adhesion to the non-adhesive areas. The fibronectin forming the circular and the square islands on the PDMS-coated glass coverslips was visualized by immunostaining. Scale bar = 50 μm. (b) Images of MSCs plated on circular or square micropatterns after cultured for 14 days in mixed differentiation medium; these were stained to reveal the presence of lipid (Oil Red O; red) and ALP activity (purple). Scale bar = 50 μm. (c) Percentage of MSCs, as indicated in (b), showing osteogenesis (ALP-positive cells) and adipogenesis (Oil Red O-positive cells). Data are mean ± s.e.m (n = 3 independent experiments). Statistical analysis of data was carried out by the Student's t-test. *$p < 0.05$; ***$p < 0.001$. (d) Fold of Runx2 total fluorescence intensity in the MSCs seeded on circular or square micropatterns after cultured for 7 days in mixed differentiation medium. Data are mean ± s.e.m [n = 27 cells (circle) and 27 cells (square) from 3 independent experiments]. Data were tested for normality and homoscedasticity in SPSS. Statistical analysis of data was carried out by the Student's t-test. ***$p < 0.001$.

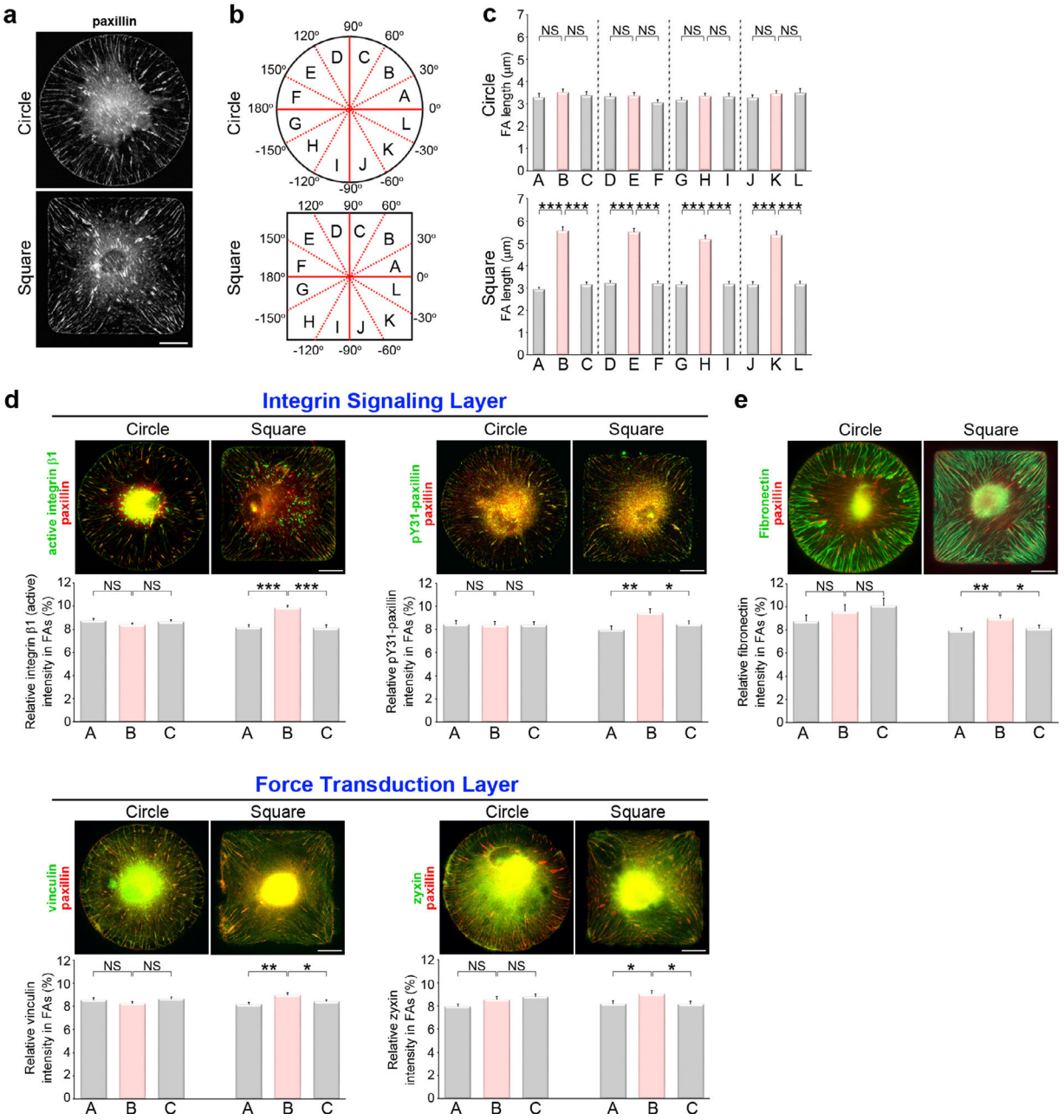

Fig. 2. Focal adhesion composition is modulated by geometric cues.

(a) Images of immunostained paxillin (to visualize FAs) in MSCs plated on circular or square micropatterns after cultured for 16 hrs in growth medium. Scale bar, 20 μm. (b) A schematic diagram of twelve angular sectors used for segmenting an imaged cell. (c) Length distribution of the paxillin-marked FAs from individual angular sectors of the MSCs, as indicated in (a). Data are mean ± s.e.m [n = 44 cells (circle) and 46 cells (square) from 3 independent experiments]. Data were tested for normality and homoscedasticity in SPSS. Statistical analysis of data was carried out by one-way ANOVA, followed by the Student's t-test. ***$p < 0.001$; NS, no significance. (d) Top: Images of immunostained paxillin and the indicated FA components within the integrin-signaling (active integrin β1 or pY31-paxillin)

and force-transduction layers (vinculin or zyxin) of the FAs in MSCs plated on circular or square micropatterns after cultured for 16 hrs in growth medium. Scale bar, 20 μm. Bottom: Percentage of the average density (intensity per μm^2) of the indicated FA protein within segmented paxillin-marked FAs in the angular sectors of the first quadrant. Data are mean ± s.e.m [active integrin β1/paxillin, n = 41 cells (circle) and 46 cells (square); pY31-paxillin/paxillin, n = 42 cells (circle) and 39 cells (square); vinculin/paxillin, n = 45 cells (circle) and 41 cells (square); zyxin/paxillin, n = 46 cells (circle) and 46 cells (square); the analyzed cells were from 3 independent experiments]. Data were tested for normality and homoscedasticity in SPSS. Statistical analysis of data was carried out by one-way ANOVA, followed by the Student's t-test. *$p < 0.05$; **$p < 0.01$; ***$p < 0.001$; NS, no significance. (e) Top: Images of immunostained paxillin and fibronectin in MSCs plated on circular or square micropatterns after cultured for 16 hrs in growth medium. Scale bar, 20 μm. Bottom: Percentage of the average density (intensity per μm^2) of fibronectin within segmented paxillin-marked FAs in the angular sectors of the first quadrant. Data are mean ± s.e.m [n = 30 cells (circle) and 29 cells (square) from 3 independent experiments]. Data were tested for normality and homoscedasticity in SPSS. Statistical analysis of data was carried out by one-way ANOVA, followed by the Student's t-test. *$p < 0.05$; **$p < 0.01$; NS, no significance.

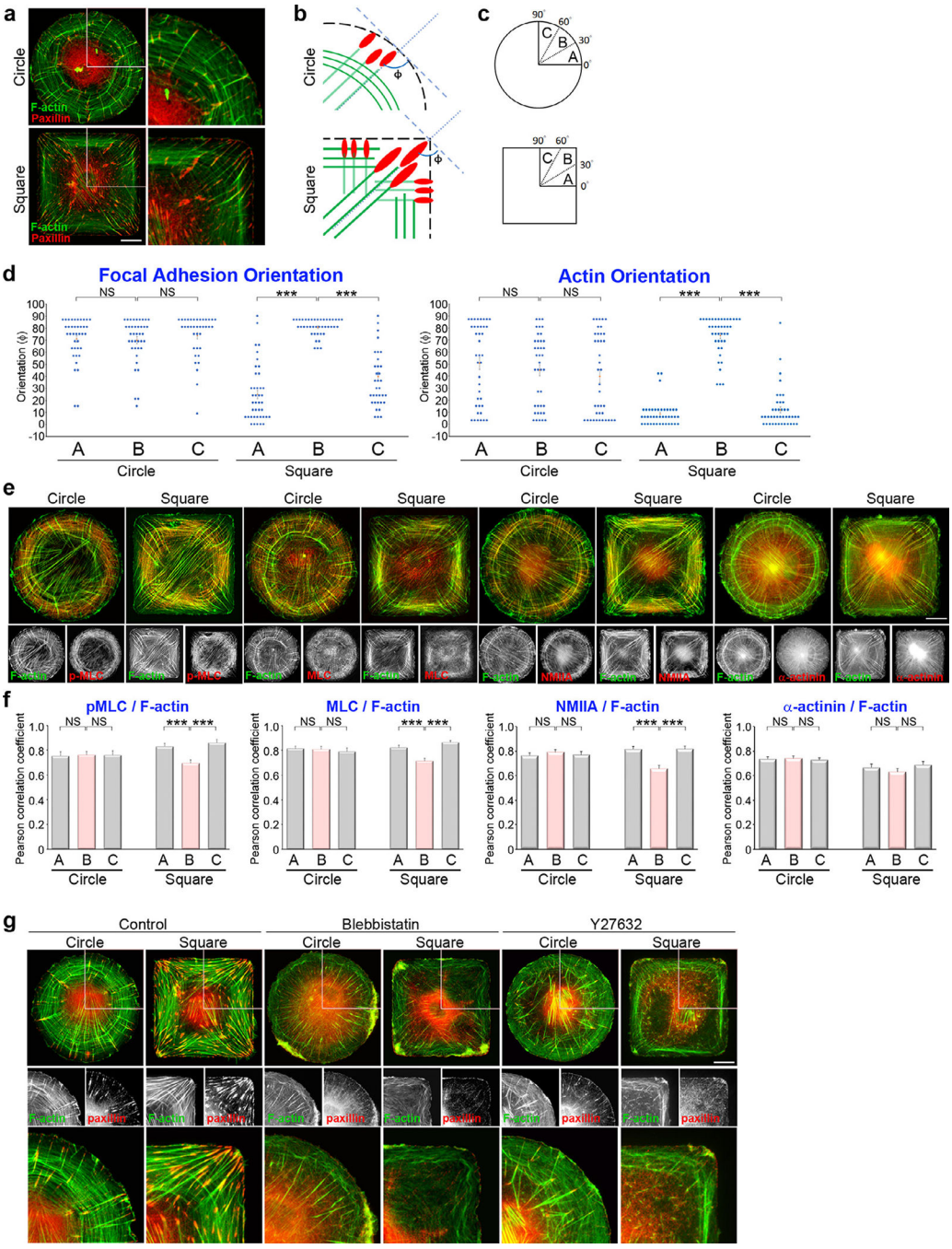

Fig. 3. Geometric cues and myosin-II mediated contractility of transverse fibers guide the alignment of focal adhesions and radial fibers.

(a) Images of immunostained paxillin and phalloidin (to visualize F-actin) in MSCs plated on circular or square micropatterns after cultured for 16 hrs in growth medium. Scale bar, 20 μm. The 53.7 μm × 53.7 μm areas indicated in the left images are magnified on the right. (b) A schematic diagram of the strategy used to determine the orientation of the indicated protein in relation to the cell edge. (c) A schematic diagram of angular sectors used for reporting statistics. (d) Orientation of the paxillin-marked FAs and F-actin in relation to the cell edge vs. angular sector for MSCs plated on circular or square micropatterns after

cultured for 16 hrs in growth medium. Data are mean ± s.e.m [F-actin, n = 39 cells (circle) and 41 cells (square); paxillin, n = 39 cells (circle) and 41 cells (square); the analyzed cells were from 3 independent experiments]. Data were tested for normality and homoscedasticity in SPSS. Statistical analysis of data was carried out by one-way ANOVA, followed by the Student's t-test. *** $p < 0.001$; NS, no significance. (e) MSCs plated on circular or square micropatterns after cultured for 16 hrs in growth medium; these were immunostained with phalloidin (to localize F-actin; green) and p-MLC (red), MLC (red), NMIIA (red) or α-actinin (red). Scale bar, 20 μm. (f) Values indicate Pearson's correlation coefficients for the images of F-actin and p-MLC, MLC, NMIIA or α-actinin, as indicated in (e), within the angular sectors of the first quadrant. Data are mean ±s.e.m [phalloidin/p-MLC, n = 40 cells (circle) and 40 cells (square); phalloidin/MLC, n = 40 cells (circle) and 49 cells (square); phalloidin/NMIIA, n = 46 cells (circle) and 46 cells (square); phalloidin/α-actinin, n = 45 cells (circle) and 45 cells (square); the analyzed cells were from 3 independent experiments]. Data were tested for normality and homoscedasticity in SPSS. Statistical analysis of data was carried out by one-way ANOVA, followed by the Student's t-test. ***$p < 0.001$; NS, no significance. (g) MSCs cultured for 16 hrs in growth medium were treated with DMSO (control), blebbistatin (50 μM, 2 h) or Y27632 (10 μM, 1h); these were immunostained for paxillin (to localize FAs; red) and phalloidin (to localize F-actin; green). Scale bar, 20 μm. The 53.7 μm × 53.7 μm areas indicated in the top images are magnified in the bottom.

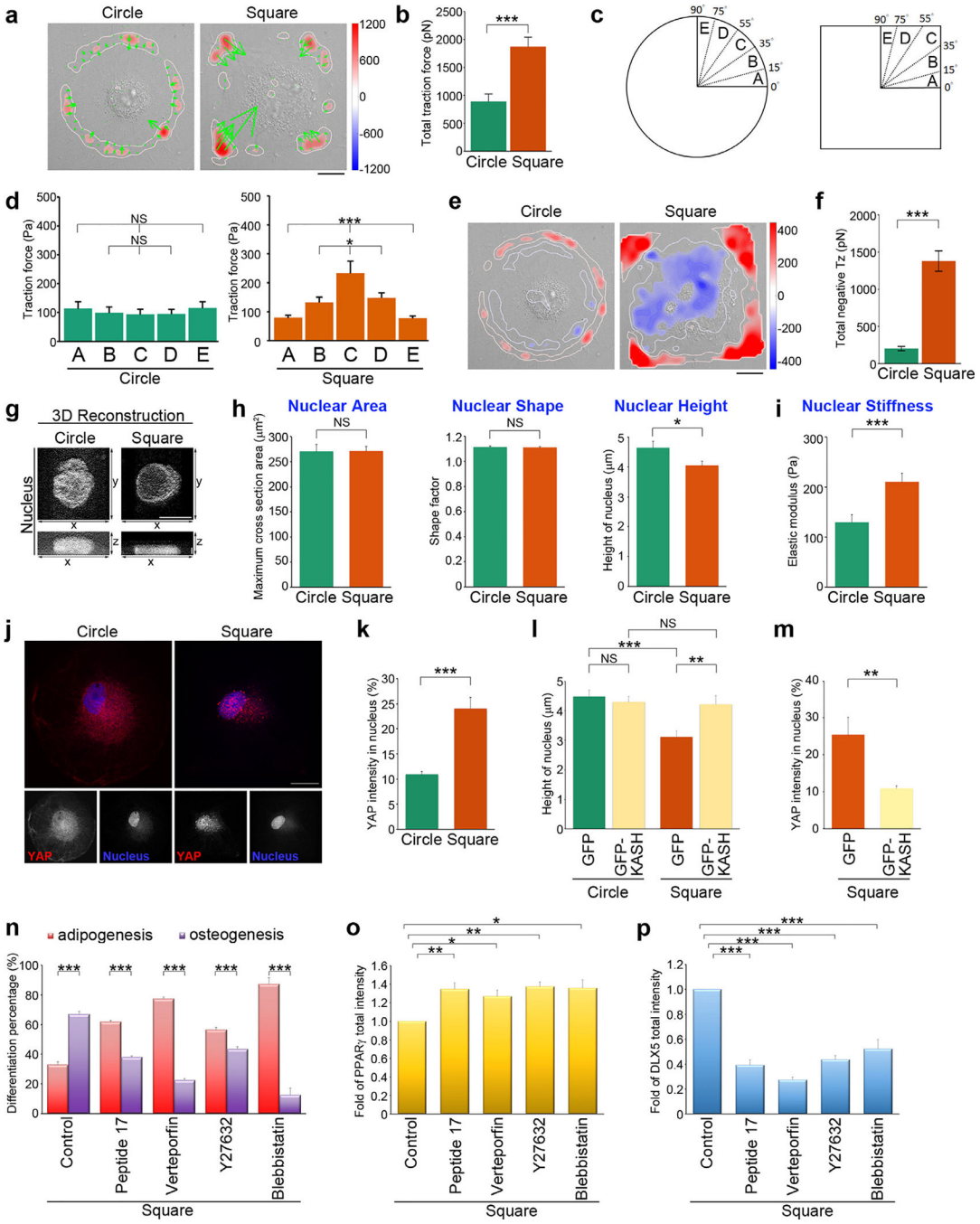

Fig. 4. Geometric cues organize the alignment of contractile force along the FA-nuclear axis to modulate nuclear stiffness and YAP nuclear localization.

(a) Image of the traction force distribution of MSCs plated on circular or square micropatterns after cultured for 16 hrs in growth medium. Scale bar, 20 μm. (b) Total traction force (pN) of MSCs, as indicated in (a). Data are mean ± s.e.m [n = 10 cells (circle) and 10 cells (square) from 3 independent experiments]. Data was tested for normality and homoscedasticity in SPSS. Statistical analysis of data was carried out by the Student's t-test. ***$p < 0.001$. (c) A schematic diagram of angular sectors used for segmenting an imaged cell. (d) Tangential traction force (Pa) at 0–15 μm from edge of MSCs, as

indicated in (a), within the angular sectors of the first quadrant. Data are mean ± s.e.m [n = 10 cells (circle) and 10 cells (square) from 3 independent experiments]. Data were tested for normality and homoscedasticity in SPSS. Statistical analysis of data was carried out by one-way ANOVA, followed by the Student's t-test. *$p < 0.05$; ***$p < 0.001$; NS, no significance. (e) Maps of out-of-plane traction stresses of MSCs plated on circular or square micropatterns after cultured for 16 hrs in growth medium. Scale bar, 20 μm. (f) Total compressive stresses (pN) of MSCs, as indicated in (e). Data are mean ± s.e.m [n = 10 cells (circle) and 10 cells (square) from 3 independent experiments]. Data were tested for normality and homoscedasticity in SPSS. Statistical analysis of data was carried out by the Student's t-test. ***$p < 0.001$. (g) 3D reconstruction taken from the z-series of confocal images of MSCs stained with DAPI (to visualize nucleus) at every 0.2 μm from top to bottom. The top view (x-y) and side view (x-z) images of the nuclei in MSCs plated on circular or square micropatterns after cultured for 16 hrs in growth medium. The top view: scale bar, 20 μm; the side view: scale bar, 2 μm. (h) Left: Projected area of the nuclei from MSCs, as indicated in (g). Data are mean ± s.e.m [n = 29 cells (circle) and 29 cells (square) from 3 independent experiments]. Data were tested for normality and homoscedasticity in SPSS. Statistical analysis of data was carried out by the Student's t-test. NS, no significance. Middle: Shape factor of nucleus from MSCs, as indicated in (g). Data are mean ± s.e.m [n = 29 cells (circle) and 29 cells (square) from 3 independent experiments]. Data was tested for normality and homoscedasticity in SPSS. Statistical analysis of data was carried out by the Student's t-test. NS, no significance. Right: Height of the nuclei from MSCs, as indicated in (g). Data are mean ± s.e.m [n = 30 cells (circle) 28 cells (square) from 3 independent experiments]. Data were tested for normality and homoscedasticity in SPSS. Statistical analysis of data was carried out by the Student's t-test. *$p < 0.05$. (i) Intranuclear elastic shear modulus (at 10 Hz; Pa) that quantified the nuclear stiffness for MSCs plated on circle or square micropatterns after cultured for 16 hrs in growth medium. Data are mean ± s.e.m [n = 30 beads/ 24 cells (circle) and 28 beads/26 cells (square) from 3 independent experiments]. Data were tested for normality and homoscedasticity in SPSS. Statistical analysis of data was carried out by the Student's t-test. ***$p < 0.001$. (j) Confocal images of MSCs plated on circular or square micropatterns after cultured for 16 hrs in growth medium; there were immunostained with YAP (red) and DAPI (to visualize nucleus; blue). Scale bar, 20 μm. (k) Percentage of YAP average density (intensity per μm^2) within nuclei of MSCs, as indicated in (j). Data are mean ± s.e.m [n = 24 cells (circle) and 31 cells (square) from 3 independent experiments]. Data were tested for normality and homoscedasticity in SPSS. Statistical analysis of data was carried out by the Student's t-test. ***$p < 0.001$. (l) Height of the nuclei from MSCs overexpressing GFP-C1 (GFP) or the GFP-Nesprin-2 (ΔN)-klarischt sequence (GFP-KASH) and plated on circular or square micropatterns after cultured for 16 hrs in growth medium. Data are mean ± s.e.m [circle, n = 22 cells (GFP) and 25 cells (GFP-KASH); square, n = 21 cells (GFP) and 25 cells (GFP-KASH); the analyzed cells were from 3 independent experiments]. Data were tested for normality and homoscedasticity in SPSS. Statistical analysis of data was carried out by the Student's t-test. **$p < 0.01$; ***$p < 0.001$, NS, no significance. (m) Percentage of YAP average density (intensity per μm^2) within the nuclei of MSCs overexpressing GFP-C1 (GFP) or the GFP-Nesprin-2 (ΔN)-klarischt sequence (GFP-KASH) and plated on square micropatterns after cultured for 16 hrs in growth medium. Data are mean ± s.e.m [n = 9 cells (GFP) and

10 cells (GFP-KASH) from 3 independent experiments]. Data were tested for normality and homoscedasticity in SPSS. Statistical analysis of data was carried out by the Student's t-test. $^{**}p < 0.01$. (n) Percentage of cells showing osteogenesis (ALP-positive cells) and adipogenesis (Oil Red O-positive cells). MSCs were plated on square micropatterns after cultured for 14 days in mixed differentiation medium containing DMSO (control), peptide 17 (2 μM), Verteporfin (10 μM), blebbistatin (50 μM) or Y27632 (10 μM). Data are mean ± s.e.m (n = 4 independent experiments). Statistical analysis of data was carried out by the Student's t-test. $^{***}p < 0.001$. (o) Fold of PPARγ total fluorescence intensity in the MSCs seeded on square micropatterns after cultured for 7 days in mixed differentiation medium containing DMSO (control), peptide 17 (2 μM), Verteporfin (10 μM), blebbistatin (50 μM) or Y27632 (10 μM). Data are mean ± s.e.m (control, n = 10 cells; peptide 17, n = 19 cells; Verteporfin, n = 26 cells; Y27632, n = 28 cells; blebbistatin, n = 25 cells; the analyzed cells were from 3 independent experiments). Data were tested for normality and homoscedasticity in SPSS. Statistical analysis of data was carried out by the Student's t-test. $^{*}p < 0.05$; $^{**}p < 0.01$. (p) Fold of DLX5 total fluorescence intensity in the MSCs seeded on square micropatterns after cultured for 1 days in mixed differentiation medium containing DMSO (control), peptide 17 (2 μM), Verteporfin (10 μM), blebbistatin (50 μM) or Y27632 (10 μM). Data are mean ± s.e.m (control, n = 20 cells; peptide 17, n = 20 cells; Verteporfin, n = 19 cells; Y27632, n = 20 cells; blebbistatin, n = 19 cells; the analyzed cells were from 3 independent experiments). Data were tested for normality and homoscedasticity in SPSS. Statistical analysis of data was carried out by the Student's t-test. $^{***}p < 0.001$.

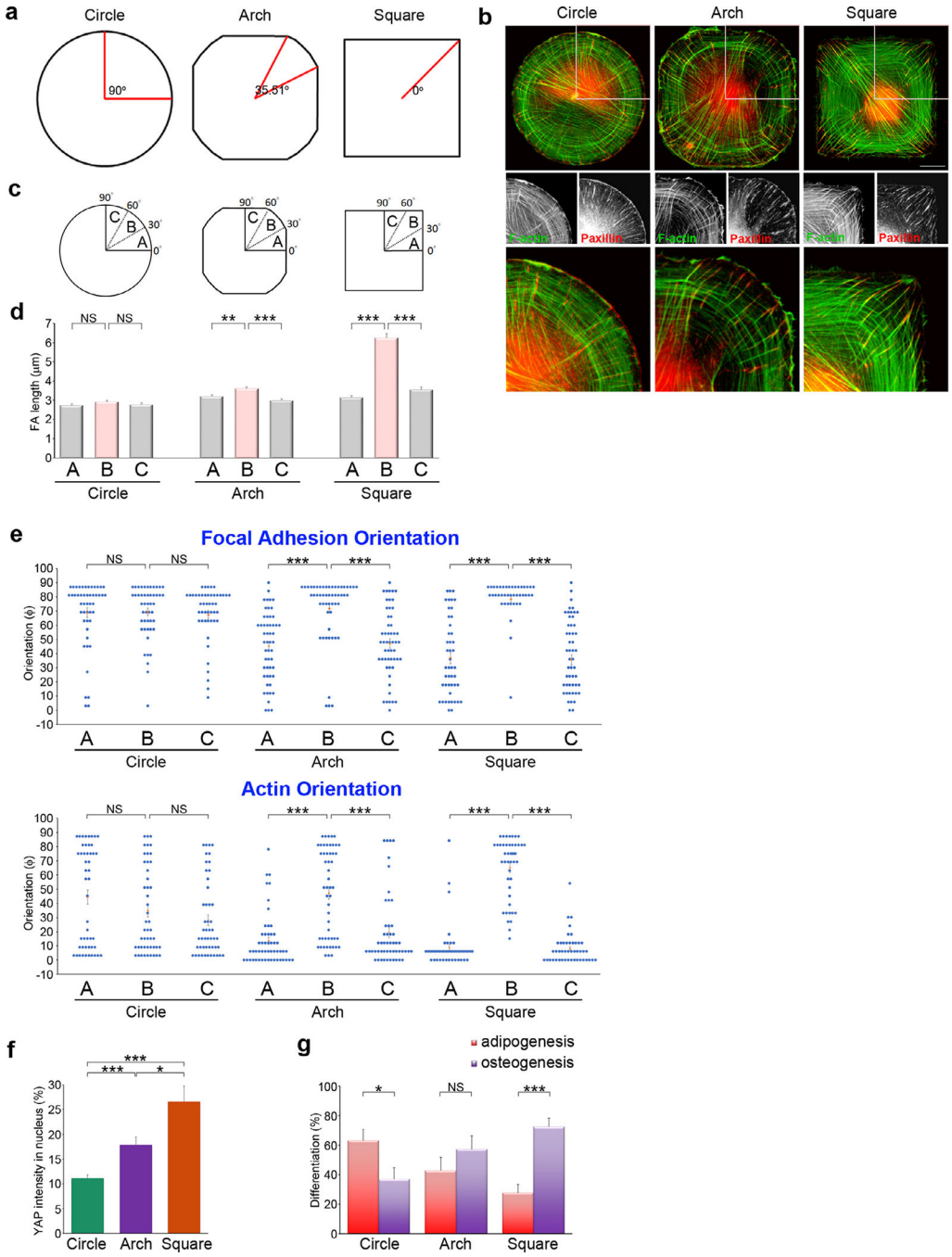

Fig. 5.

Cell's sharp corners guide the alignment of focal adhesions and bundle actin filaments to transmit contractile forces from FAs to the nucleus.

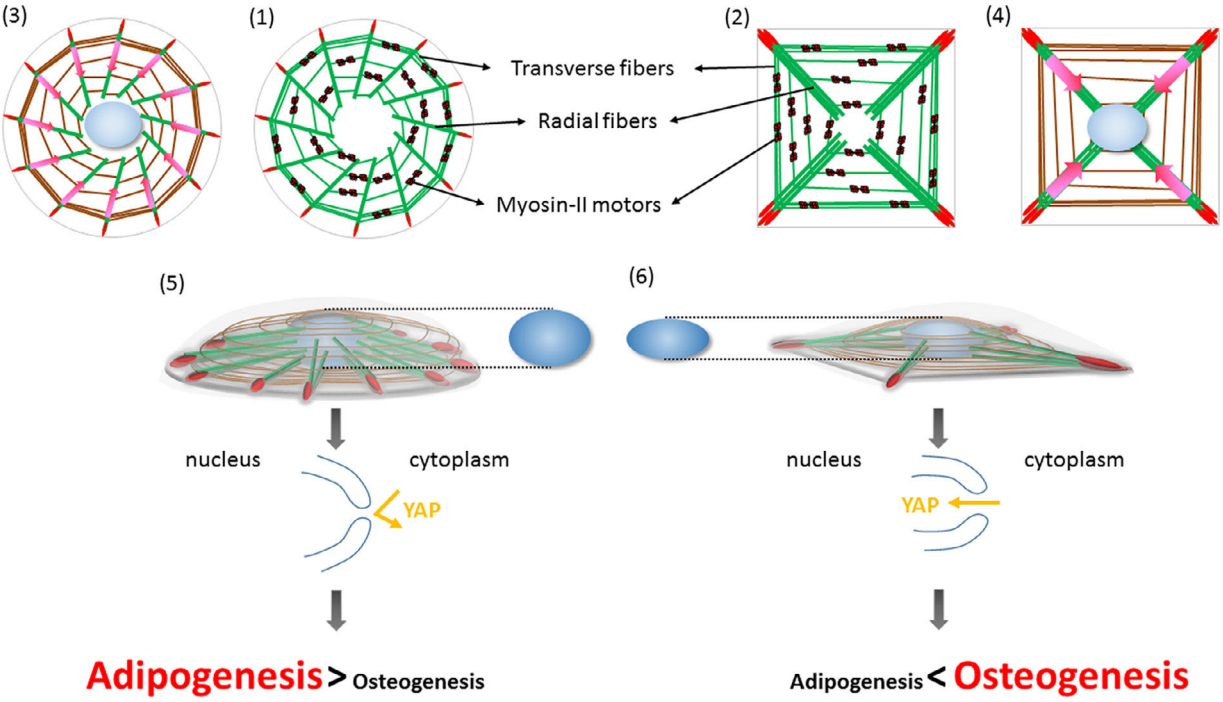

Fig. 6. A proposed model for the effects of high-curvature cell shape regions on FA-actin organization, nuclear deformability, and lineage commitment of MSCs.

MSCs plated on circular and square micropatterns form circular cells (71) and square cells (2), respectively. FAs sense substrate topography, which in turn changes the protein composition of the FAs and guide the orientation of the radial fibers. The radial fibers are bound to the ends of the transverse fibers, which predominantly contain myosin-II motor proteins to generate contractile forces. In circular (3) and square cells (4), actomyosin contractility causes a centripetal motion of the transverse fibers, which pull the radial fibers and transmit the forces to the FAs; this creates a global centripetal flow within the actin system. The radial configuration of the actin system in circular (5) and square cells (6) brings about nuclear deformation in the latter case and this regulates YAP nuclear translocation, which in turn dictates MSC lineage commitment.